MATEMATICKO-FYZIKÁLNÍ
FAKULTA
Univerzita Karlova

BAKALÁŘSKÁ PRÁCE

Zsolt Beke

Analýza mikrostruktury a mechanismů plastické deformace vysokopevných Mg-Zn-Y slitin

Katedra fyziky materiálů

Vedoucí bakalářské práce: RNDr. Daria Drozdenko, Ph.D.

Studijní program: Fyzika

Studijní obor: Obecná fyzika

Praha 2024

FACULTY
OF MATHEMATICS
AND PHYSICS
Charles University

BACHELOR THESIS

Zsolt Beke

Analysis of microstructure and mechanisms of plastic deformation of high-strength Mg-Zn-Y alloys

Department of Physics of Materials

Supervisor of the bachelor thesis: RNDr. Daria Drozdenko, Ph.D.

Study programme: Physics

Specialization: General physics

Prague 2024

I declare that I carried out this bachelor thesis independently, and only with the cited sources, literature and other professional sources.

I understand that my work relates to the rights and obligations under the Act No. 121/2000 Coll., the Copyright Act, as amended, in particular the fact that the Charles University has the right to conclude a license agreement on the use of this work as a school work pursuant to Section 60 paragraph 1 of the Copyright Act.

In…..... date..... signature

In this place I would like to express my biggest gratitude to my supervisor Dr. Daria Drozdenko for her help, patience and guidance through the whole year. I am grateful to prof. Kristian Mathis for introducing me to the field of material sciences and for the useful ideas. My sincere thanks go to Dr. Gergely Németh and Dr. Gergely Farkas for sacrificing their time to help with the diffraction data evaluation. I am also grateful to Mgr. Andrea Farkas for providing a helpful hand by the microstructure measurements using the SEM. The last but not least, I would like to thank to my family and friends for their support and faith in me.

Title: Analysis of microstructure and mechanisms of plastic deformation of high-strength Mg-Zn-Y alloys

Author: Zsolt Beke

Department / Institute: Department of Physics of Materials, Faculty of Mathematics and Physics, Charles University

Supervisor of the bachelor thesis: RNDr. Daria Drozdenko, Ph.D., Department of Physics of Materials

Abstract: This thesis in focused on revealing deformation mechanisms resulting in high-strength and moderate elongation of the $Mg_{97.94}Zn_{0.56}Y_{1.5}$ (at. %) alloys prepared by rapidly solidified ribbon consolidation technique. The processing method alongside with low alloying content results a fine-grained microstructure with Zn- and Y-rich stacking faults formed in the basal planes. In addition, the extruded from cast ingot alloys of the same composition, characterized by homogeneous microstructure with large gains and presence of long-period stacking order (LPSO) phase have been used as a reference material. The latter alloys are showing better ductility but lower strength compared to the rapidly solidified ribbon consolidated alloys. Besides, the effect of extrusion ram speed on microstructure and resulting mechanical properties is addressed. Microstructure observations has been performed using light and scanning electron microscopy. Lower values of yield strength in tension compared to that in compression motivated further detailed investigation using advanced technique. Thus, *in-situ* synchrotron X-ray diffraction method has been employed for analysis of the deformation mechanisms, indicating the activation of non-basal slip systems alongside the primary basal slip system, with negligible twinning. Moreover, particular attention has been paid to revealing background mechanisms leading to yield point phenomenon.

Keywords: magnesium, microstructure, mechanical properties, X-Ray diffraction

Název práce: Analýza mikrostruktury a mechanismů plastické deformace vysokopevných Mg-Zn-Y slitin

Autor: Zsolt Beke

Katedra / Ústav: Katedra fyziky materiálů, Matematicko-fyzkální fakulta, Univerzita Karlova

Vedoucí bakalářské práce: RNDr. Daria Drozdenko, Ph.D., Katedra fyziky materiálů

Abstrakt: Tato práce se zaměřuje na odhalení mechanismů deformace vedoucích k vysoké pevnosti a zároveň zlepšenou tvarovatelnost $Mg_{97.94}Zn_{0.56}Y_{1.5}$ (at. %) slitin, připravených technikou rychlé solidifikace. Způsob zpracování a použití slitin s nízkým obsahem legujících prvků vede k formováni jemnozrnné mikrostruktuře s Zn- a Y- vrstvovými chybami v bazálních rovinách. Kromě toho byly jako referenční materiál použity odlévané a pak extrudované slitiny stejného složení, které mají homogenní mikrostrukturu s větším zrnem a přítomností fáze s dlouhoperiodickým uspořádáním (angl. LPSO). Tyto slitiny vykazují vyšší tažnost, ale nižší pevnost ve srovnání se slitinami připravenými rychlou solidifikace. V rámci práce byl také studován vliv rychlosti extruze na mikrostrukturu a výsledné mechanické vlastnosti. Pozorování mikrostruktury bylo provedeno pomocí světelné a skenovací elektronové mikroskopie. Nižší hodnoty mezí kluzu při tahovém zatěžování ve srovnání s tlakovým zatížením podnítily další detailní zkoumání pomocí moderních a pokročilých technik. Byla proto využita metoda *in-situ* synchrotronové rentgenové difrakce pro analýzu mechanismů deformace. Výsledky poukázali na aktivaci nebazálních skluzových systémů vedle primárního bazálního skluzového systému, s nepatrným vyskytováním dvojčátení. Kromě toho byla věnována zvláštní pozornost odhalení pozadí mechanismů vedoucích k fenoménu mezního bodu kluzu (angl. yield point phenomenon).

Klíčová slova: hořčíkové slitiny, mikrostruktura, mechanické vlastnosti, rentgenová difrakce

Contents

Introduction

Nowadays, the demand in automotive and aircraft industries for lightweight materials is greater than ever. The main goal is to fabricate weight reduced, environmentally friendly, cheap and certainly safe vehicles. Stating the obvious, the lighter vehicles have smaller fuel consumption, thus reduces the CO_2 emission. It was reported that reducing the weight of the vehicles by 10% results in reduced fuel consumption by approximately 5 % [1]. Magnesium alloys are a great candidate because of the low density and high strength-to-weight ratio [2]. Although magnesium does not occur in nature in the metallic form, commercial amounts of magnesium ores are found worldwide. Magnesium is the eighth most abundant element is the Earth's crust, making up 13% of the planet's mass [3]. Also, for recycling only 5% of the energy used for production is required. By 1900, worldwide production of magnesium had reached only 10 tonnes per year this number increased to more than 30 000 tonnes per year by 1939 [4]. In mass production it was first used by Volkswagen in the 1930s. In the model Beetle the magnesium cast parts weighted a total of 17 kg, which was said to represent a savings of 50 kg when compared with cast iron [4]. Moreover, the biocompatibility of magnesium (the value of Young modulus is close to one for the bones) further encourages its advancement as a biomaterial for implants. On the other hand, their application is limited due to low formability, low yield strength and unstable corrosion behaviour. Some of these disadvantages can be reduced by alloying elements. The recently developed Mg-Zn-Y-based alloys gained significant attention because of their excellent mechanical properties at room and elevated temperature compared to conventional alloys [5,6]. In general, the prominent mechanical properties of these alloys are obtained thanks to the coexistence of the fine recrystalized and coarse worked grains [7]. Further, modern processing techniques, such as rapidly solidified ribbon consolidation, were found to be beneficial for developing novel magnesium alloys with even more enhanced properties.

This work is focused on revealing the active deformation mechanisms in high-strength dilute Mg-Zn-Y-based alloys prepared by rapidly solidified ribbon consolidation technique.

1. Theoretical background

1.1. Magnesium alloys and active deformation mechanisms

Magnesium (Mg) is one of the lightest metals. Pure Mg has a melting point at 650 °C under atmospheric pressure and density of 1.738 gcm^{-3} [4]. This metal has a hexagonal closed packed (hcp) crystal lattice with two parameters characterizing the crystallographic structure - lattice parameters, a and c, see Figure 1.1. Parameter a indicates the distance between two atoms in the basal plane, and c is the distance between two atoms perpendicular to the basal plane. In materials with an hcp structure the plastic deformation strongly depends on the ratio c/a. The ideal value is $c/a = \sqrt{8/3} = 1.633$, which is the closest configuration for hcp crystal structure with perfectly spherical atoms. Pure Mg is characterized by value of 1.623, what is the closest value to ideal one [8].

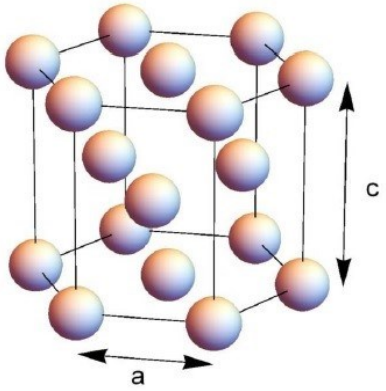

Figure 1.1. Hexagonal closed packed lattice [9].

In hcp crystals the elementary plastic deformation mechanisms are dislocation slip and twinning. Dislocation slip refers to the process by which dislocations move through a crystal lattice. Dislocation is a line defect which can be categorized depending on the direction of the shear stress to edge and screw dislocations (see Figure 1.2.). An edge dislocation can be presented by inserting a half plane of atoms in a perfect crystal lattice. The edge of this embedded half plane is the dislocation edge. Screw dislocation can be imagined by cutting the crystal along the atomic plane and moving one part parallel to the dislocation edge.

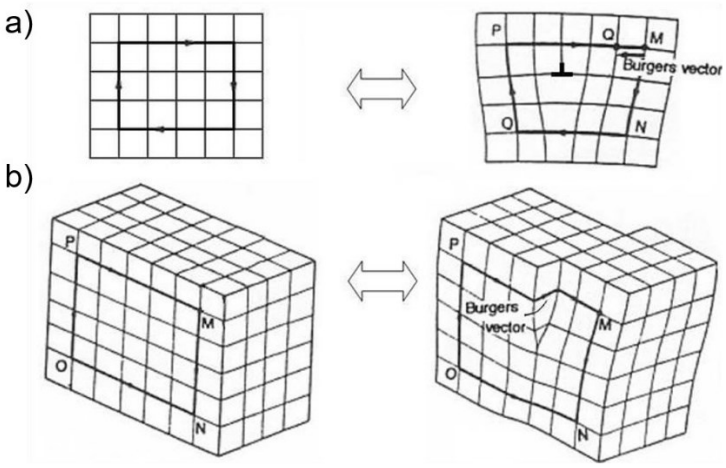

Figure 1.2. Illustration of (a) edge and (b) screw dislocation type [10].

A slip system describes the set of symmetrically identical slip planes and family of slip directions where dislocations can move. The magnitude and the direction of slip are represented by the Burgers vector. The main slip systems of materials with hcp structure are following: basal, prismatic and pyramidal (Figure 1.3).

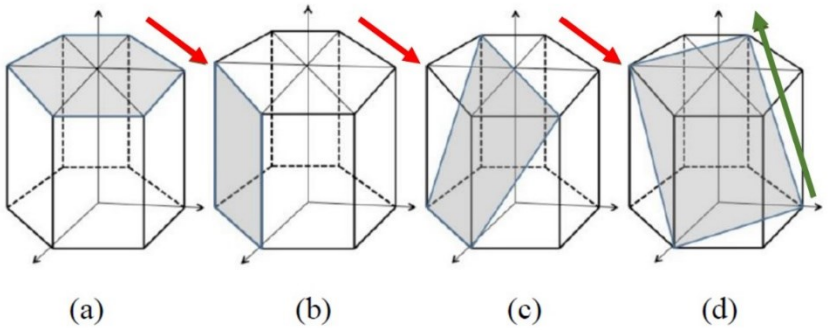

Figure 1.3. The main slip systems in hcp metals: a) basal, b) prismatic, c) first order pyramidal and d) second order pyramidal slip systems. The red arrows indicate the <a> direction and the green one the <c+a> direction [11].

As has been mentioned above, the mechanisms of the plastic deformation strongly depend on the ratio of the crystallographic axis c/a. Particularly, if c/a is smaller than the ideal value, the atomic density of basal lattice planes decreases, therefore the slip takes place primary in non-basal planes due to the lower activation energy. This can be observed for titanium and zirconium and their alloys. On the

contrary, if c/a is larger than the ideal value the slip takes place primary in the basal plane. This is characteristic for zinc and cadmium. In case of Mg, the *c/a* ratio is close to the ideal value, therefore besides primary basal (0001) slip, the prismatic {10-10} and pyramidal first order {10-11} slip in the directions <11-20> (the so-called <a> type slip systems) can be activated [12]. However, according to the von Mises criterion, for a homogeneous plastic deformation of the polycrystalline materials, at least 5 independent slip systems are required [13]. Therefore, to fulfil the von Mises criterion additional slip system needs to be activated in Mg and its alloys. The deformation along <c> axis is achievable by the activation of second order pyramidal slip system {11-22} in the direction <11-23> (<c+a> type slip system) or by twinning mechanism. The most common twinning mechanism in Mg alloys is the so-called extension twinning, which is activated when external compression loading applied perpendicular to *c*-axis, and newly created fraction (twin) is characterised by misorientation of 86° with respect to the original lattice [14].

The activation of slip systems is strongly orientation dependent. This fact was firstly characterized by Schmid [15]. A slip occurs on certain preferred planes characterized by the highest Schmid factor (max value is 0.5), which is defined as

$$m = cos\varphi cos\lambda, \tag{1}$$

where φ is the angle between the loading axis and the normal to slip plane and λ is the angle between the loading axis and the slip direction, see Figure 1.4.

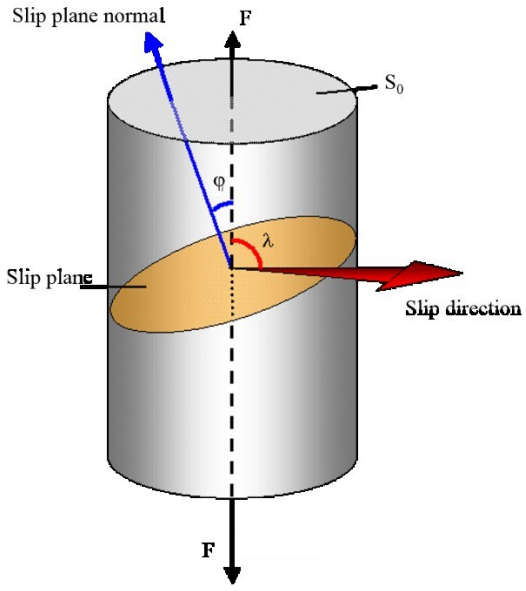

Figure 1.4. Illustration of the dislocation slip in a crystal [8].

From equation (1) it is obvious that when the particular plane is parallel to the loading axis, the Schmid factor is 0. Therefore, if the basal plane is almost parallel to the loading axis, the Schmid factor is close to 0 and deformation can hardly proceed by basal slip. In this case, deformation is realized by twinning or by slip on non-basal planes, when required critical resolved shear stress (CRSS) for the given slip system is achieved. It should be also noted, that CRSS for basal slip is lowest within possible slip systems in Mg alloys, whereas significantly higher stress must be applied for the activation of prismatic and pyramidal slip systems compared to the basal slip or twinning activation.

1.2. High-strength Mg-Zn-Y-based alloys

Alloying elements are used for modifying microstructure and thus resulting properties of the pure Mg. By adding the appropriate elements - for example rare earth elements - strength, elastic modulus and corrosion resistance can be improved. Particularly, the recently developed Mg-Zn-Y alloys have outstanding mechanical properties because of the coexistence of long-period stacking order (LPSO) phase, dynamically recrystalized (DRX) and coarse non-DRX α-Mg grains [7,16]. The fine DRX grains support the ductility, and the coarse non-DRX grains contribute to the strength together with the LPSO phase [7]. The LPSO phase has interesting impact on the performance of the alloys. Presence of the LPSO phase leads to suppression of twinning activity, while another deformation mechanism – kinking – can be activated in LPSO fractions contributing to strengthening of the alloy. Thus, higher volume fraction of the LPSO phase yields higher strength [8, 16].

At the same time, to obtain better mechanical properties for practical use, modern processing techniques have been developed. For example, application of rapidly solidified ribbon consolidation (RSRC) technique for dilute Mg-Zn-Y alloys (i.e. with the low amount of alloying elements) led to formation ultrafine grained microstructure with dispersed solute segregated staking faults (SFs) and/or cluster arranged layers (CALs) of solute-enriched SFs in α-Mg matrix instead of complete LPSO phase [17, 18, 19]. Developed microstructure is resulting in extremely high yield strength with moderate elongation [5, 17].

2. Aims of the thesis

The main goal of this work is a thorough description of the active deformation mechanisms in high-strength dilute Mg-Zn-Y-based alloys prepared by a RSRC technique. A comprehensive characterization of the microstructure development required to genuine understanding of deformation mechanisms will be performed using advanced experimental methods, such as *in-situ* synchrotron X-ray diffraction and scanning electron microscopy. To achieve the main goal, the following particular tasks have to be accomplished:

- Characterization of the initial microstructure and texture of the $Mg_{97.94}Zn_{0.56}Y_{1.5}$ alloys with respect to the processing technique (RSRC vs hot extrusion) and its parameter (extrusion ram speed).
- Analysis of the mechanical properties of the investigated alloys with respect to microstructure given by processing technique.
- Revealing of the active deformation mechanism during tension of high-strength dilute RSRC alloy using *in-situ* synchrotron X-ray diffraction.

3. Material and experimental methods

3.1. Investigated alloys

For the purpose of this work, the $Mg_{97.94}Zn_{0.56}Y_{1.5}$ (at. %) alloy was prepared by gravity casting in an Ar atmosphere. To ensure the best possible corrosion resistance the ratio of Y/Zn amount was set to 2.66 according to [20]. Considering economic reasons and biocompatibility of developed alloys, the composition with reduced amount of alloying elements (up to 1.5 at. %) has been selected. The RS ribbons were prepared by a single roller liquid quenching melt-spinning method [15] at a roll peripheral speed of 42 m/s and a cooling rate of $1.4 \cdot 10^5$ K/s. Afterwards, the RS ribbons were consolidated by following procedure: cold compacting into a copper billet (with an applied pressing stress of about 25 MPa), degassing at 523 K for 15 min, and extrusion with extrusion ratio R10 at 623 K and extrusion ram speed of 5.0 mm/s and 6.7 mm/s, hereafter RS 5.0 and RS 6.7, respectively. To reveal the effect of the microstructure given by the processing on mechanical properties, the alloy with the same composition ($Mg_{97.94}Zn_{0.56}Y_{1.5}$ (at. %)) was produced by hot extrusion directly from gravity cast ingot with the same extrusion ratio and ram speed of 5.0 and 6.7 mm/s (hereafter CE 5.0 and CE 6.7, respectively) and subjected to further investigation.

3.2. Light microscopy

The microstructure of the investigated materials was studied by light microscopy (LM) using the Olympus GX51 microscope. For microstructure observation, the alloys were cut by the BRILLANT 220 QATM cut-off machine to get samples representing the cross- and longitudinal sections of the extruded bar, i.e., perpendicular (hereafter, cross section) and along the extrusion direction (ED), respectively. Samples were manually ground on SiC papers and then using diamond pasted with a size down to 0.25 μm for the purpose of getting a smooth surface. In order to reveal grain boundaries, polished surfaces were etched in a solution of 50 ml ethanol, 9 ml water, 4 ml acetic acid, and 6 g picric acid for approximately 10 s.

3.3. Scanning electron microscopy

More detailed investigation of the microstructure with higher resolution was performed by scanning electron microscopy (SEM) using Quanta FEI 200 FEG, Apreo 2 Thermofisher and Zeiss Auriga Compact microscopes. Backscattered electrons (BSE) are used to reveal presence and distribution of solute-enriched SFs and CALs, because they are sensitive to the atomic number of the nuclei they scatter from. Heavy elements scatter electron more likely than lighter elements (e.g., Zn and Y in contrast to Mg), therefore in BSE images they have brighter contrast. The electron back-scattered diffraction (EBSD) method was used reveal the size and orientation of the grains. Orientation maps were collected with a step of 0.3 μm (CE samples) and 40 nm (RS samples) and an acceleration voltage of 15 kV. The maps were evaluated with the OIM software. Before investigating, the samples were manually polished using SiC papers and diamond pastes, followed by polishing with argon ions for 1 hour in Leica EM RES102.

The EBSD map displays only a small area of the investigated alloy. Thus, to represent the texture of the material, large scan should be obtained from several areas. To avoid this, the textures of the alloys were calculated from the diffraction data, which reveals information from larger volume, therefore obtained results are more reliable. The textures of the materials were calculated using python's LMFIT library. Afterwards the inverse pole figures (IPF) were plotted using MATLAB software's MTEX toolbox [21].

3.4. Deformation tests

Mechanical properties of the investigated alloy were studied in tension and compression at RT with a constant strain rate of $5 \cdot 10^{-4}$ s^{-1} using the Instron 5882 universal testing machine. For tensile tests, samples with a gauge length of 24 mm, a diameter of 4 mm, and screw heads on both ends were machined from the as-received bars parallel to ED. For compression tests, cylindrical samples with a height of 10 mm, a diameter of 5 mm were machined from the as-received bars parallel to ED.

3.5. *In-situ* synchrotron X-ray diffraction

X-ray diffraction is a powerful method revealing the microstructure and the deformation properties of materials. X-rays generated by synchrotron are more intense than the laboratory sources, therefore their usage is preferrable at analysing of the microstructure when acquisition time is critically important, e.g. during mechanical loading.

The basic principle of the X-ray technique is that the incident beam diffracts on the periodically spaced lattice planes according to the Bragg's law:

$$\lambda = 2d_{hkl}sin(\theta_{hkl}), \tag{2}$$

where λ is the wavelength of the X-Rays, d_{hkl} is the lattice spacing (distance between neighbour atomic spaces) with indices h, k, l, and θ_{hkl} is the Bragg angle between the incident wave and the atomic plane where the diffraction takes place. Diffraction provides information only from the planes which are perpendicular to the diffraction vector q which is defined by

$$q = k_0 - k, \tag{3}$$

where k_0 is the initial wave vector and k is the diffracted vector (see Figure 3.1).

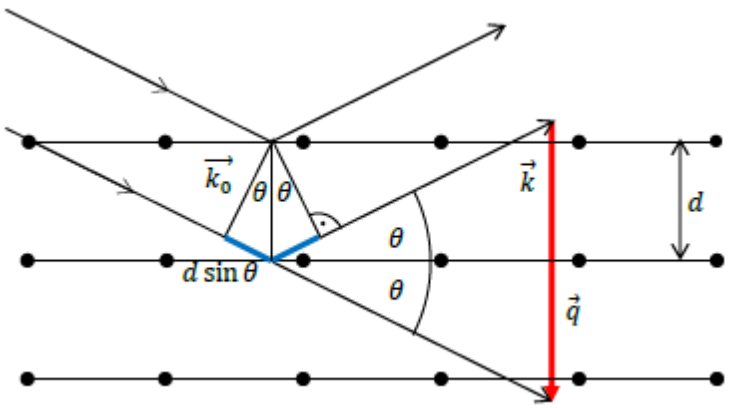

Figure 3.1. Bragg's diffraction on periodically spaced planes [22].

If the incident wave is monochromatic, the d-spacing can be calculated from the positions of the diffraction peaks using Bragg's law. During deformation, a change

in the lattice spacing can take place. This causes a shift of the diffraction peak positions in the diffractogram. From this shift, the lattice strain ε_{hkl} can be calculated as

$$\varepsilon_{hkl} = \frac{d_{hkl} - d_{0,hkl}}{d_{0,hkl}}, \tag{4}$$

where d_{hkl} is the lattice spacing for a plane with the given Miller indices when the crystal is under deformation and $d_{0,hkl}$ is the planar spacing for a crystal in initial state.

In order to follow microstructure development during mechanical loading and reveal active deformation mechanisms, the *in-situ* synchrotron diffraction measurements during tensile loading at RT with a constant strain rate of $5 \cdot 10^{-4}$ s^{-1} were carried out on the P07- HEMS (High Energy Materials Science) beamline of Petra III at DESY (Deutsches Electronen-Synchrotron), Hamburg, Germany. The experimental setup is shown in Figure 3.2.

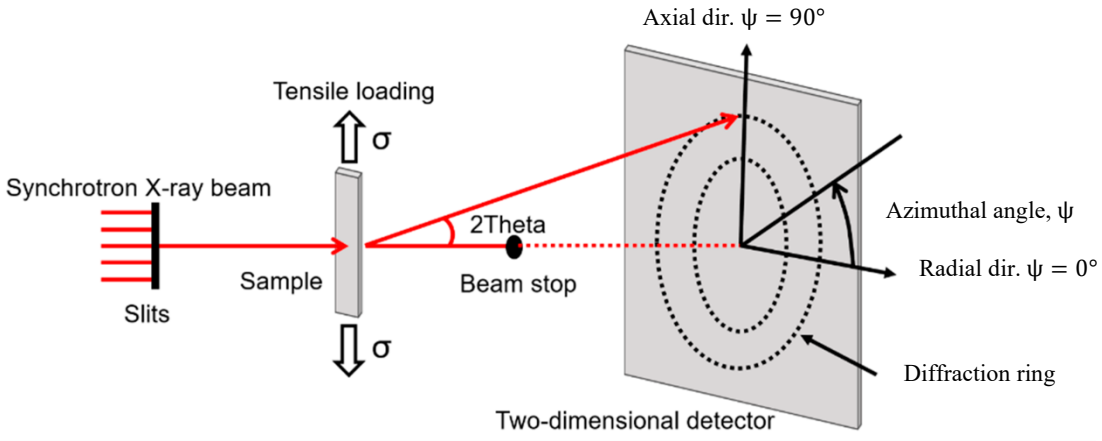

Figure 3.2. The experimental setup for the in-situ diffraction measurements during deformation tests. ψ *is the azimuthal angle [23].*

A monochromatic X-ray beam with a wavelength of $\lambda = 0.1258$ Å ($E = 98.5$ keV) was used. The diffraction patterns were recorded by a Perkin-Elmer XRD 1622 detector with an array of 2048^2 pixels. The effective pixel size was 200 x 200 μm^2. To calibrate the diffraction spectra a LaB6 standard sample was used. The distance between the sample and detector was set to 1621 mm. The measured Debye-Scherrer rings were azimuthally integrated using a Python library pyFAI [24]

in order to obtain the diffraction data. Afterward, in order to determine the peak positions and other important parameters, the acquired data in axial direction were fitted using python's LMFIT library with Voigt functions [25]. For the next data evaluation and for presenting the obtained results, the OriginPro software was used. The elastic (lattice) strain was calculated by the relative shifts in the peak positions as it was mentioned before. Inserting equation (2) to equation (4) the elastic strain can be expressed as

$$\varepsilon_{hkl} = \frac{sin(\theta_{0,hkl})}{sin(\theta_{hkl})} - 1, \tag{4.1}$$

where the angles $\theta_{0,hkl}$ and θ_{hkl} are the diffraction angle of the *hkl* plane in the stressed and stress-free crystal as has been mentioned above.

4. Results

4.1. Characterization of the initial microstructure

The initial microstructure was investigated by a LM and SEM. In order to reveal microstructure with respect to geometry of the sample, the images were taken at cross and longitudinal sections, i.e., perpendicular and along ED. Particularly, the images obtained by LM were obtained only from the longitudinal sections (Figures 4.1 - 4.2), while BSE images were obtained in both directions (Figures 4.3- 4.4). Figure 4.1 indicates that, independently on extrusion speed, the CE samples are characterized by homogeneous microstructure with the LPSO phase fractions elongated in ED. At the same time, the RS alloys are characterized by a bimodal microstructure with fine DRX grains and coarse non-DRX grains elongated in ED, see Figure 4.2.

a) b)

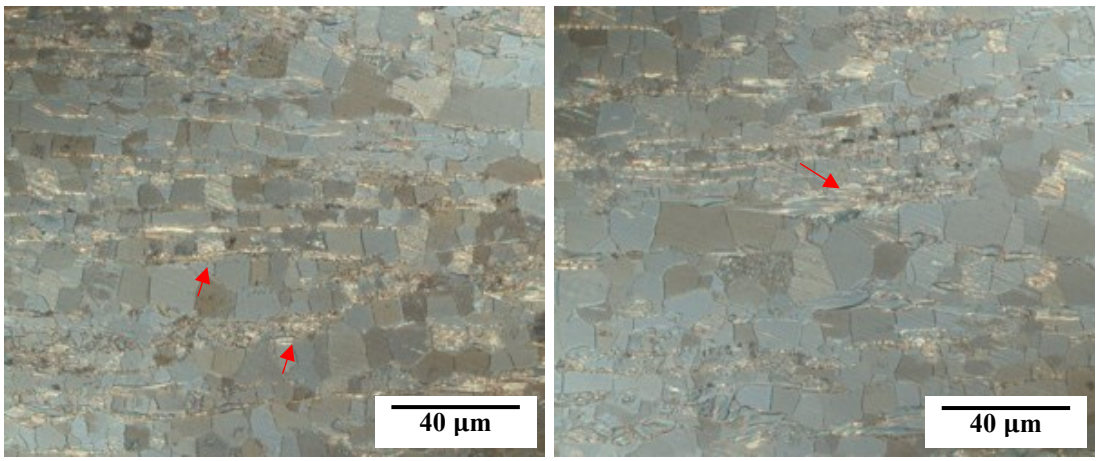

Figure 4.1. The initial microstructure of the (a) CE 5.0 and (b) CE 6.7 alloys obtained by LM. ED is horizontal. The LPSO phase is marked by red arrows.

a) b)

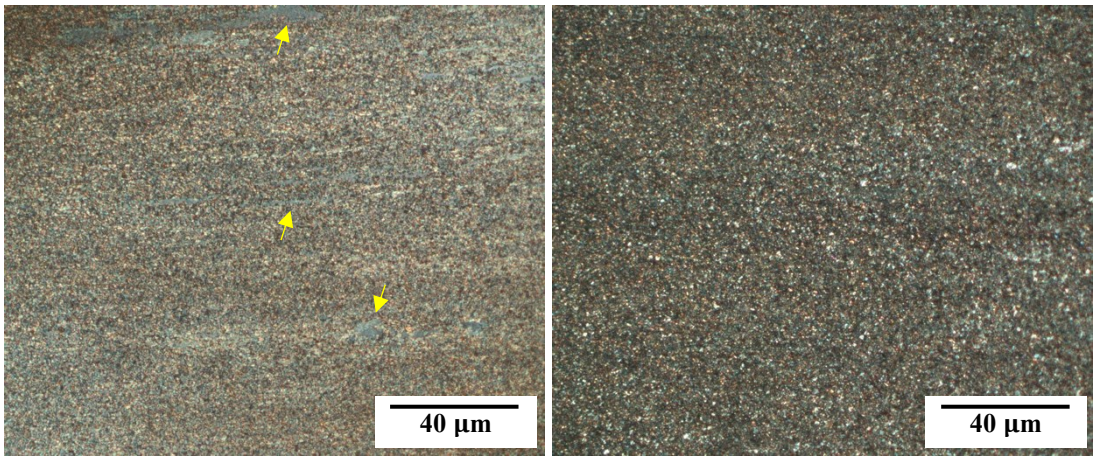

Figure 4.2. The initial microstructure of the (a) RS 5.0 and (b) RS 6.7 alloys obtained by LM. ED is horizontal. Non-DRX grains are marked by yellow arrows.

The BSE images, presented in Figures 4.3-4.4, support main tendencies regarding microstructure characteristic revealed by LM. Moreover, the brighter contrast of BSE images indicates the enrichment by Zn and Y elements, because of the higher atomic weight than the Mg. The darker contrast corresponds to the Mg matrix. Therefore, brighter contrast of larger fractions in Figure 4.3 confirms presence of the LPSO phase in CE samples. Majority of LPSO fractions is formed at the grain boundaries and is elongated along ED. In case of RS samples (Figure 4.4), the enriched

fractions are significantly smaller comparing to the LPSO phase in the CE alloys. In contrast to the LPSO phase formed at the grain boundaries in the CE alloys, the solute segregated SFs and/or CALs formed from solute-enriched SFs are dispersed in the interior of the DRX α-Mg grains of RS alloys, as can be seen in Figure 4.4. There is no orientation alignment of SFs and/or CALs with respect to the sample geometry. No significant difference in the microstructure with respect to variation in the extrusion speed has been observed in both the CE and RS alloys.

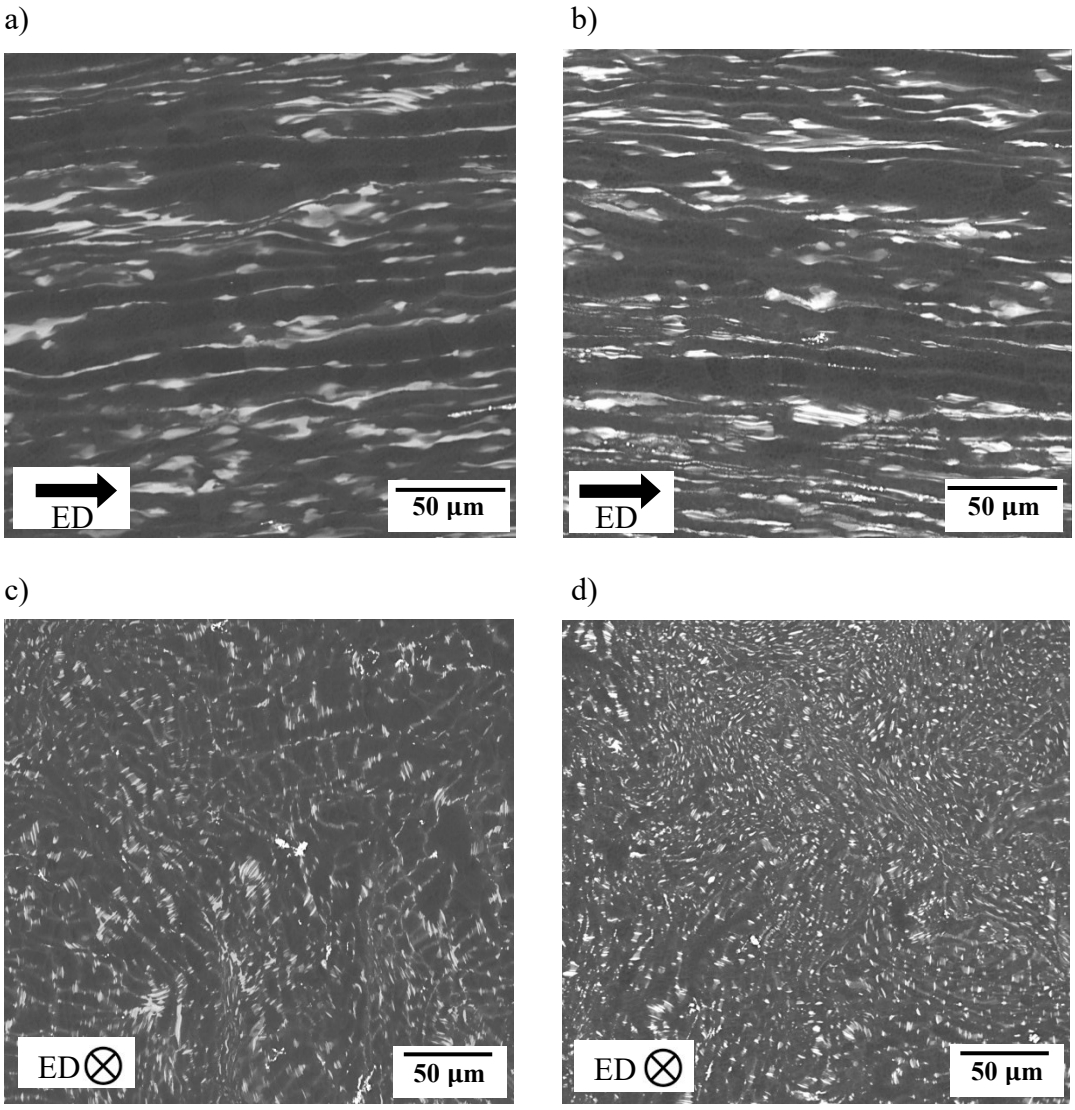

Figure 4.3. BSE images of the (a,c) CE 5.0 and (b,d) CE 6.7 samples in longitudinal and cross section, respectively.

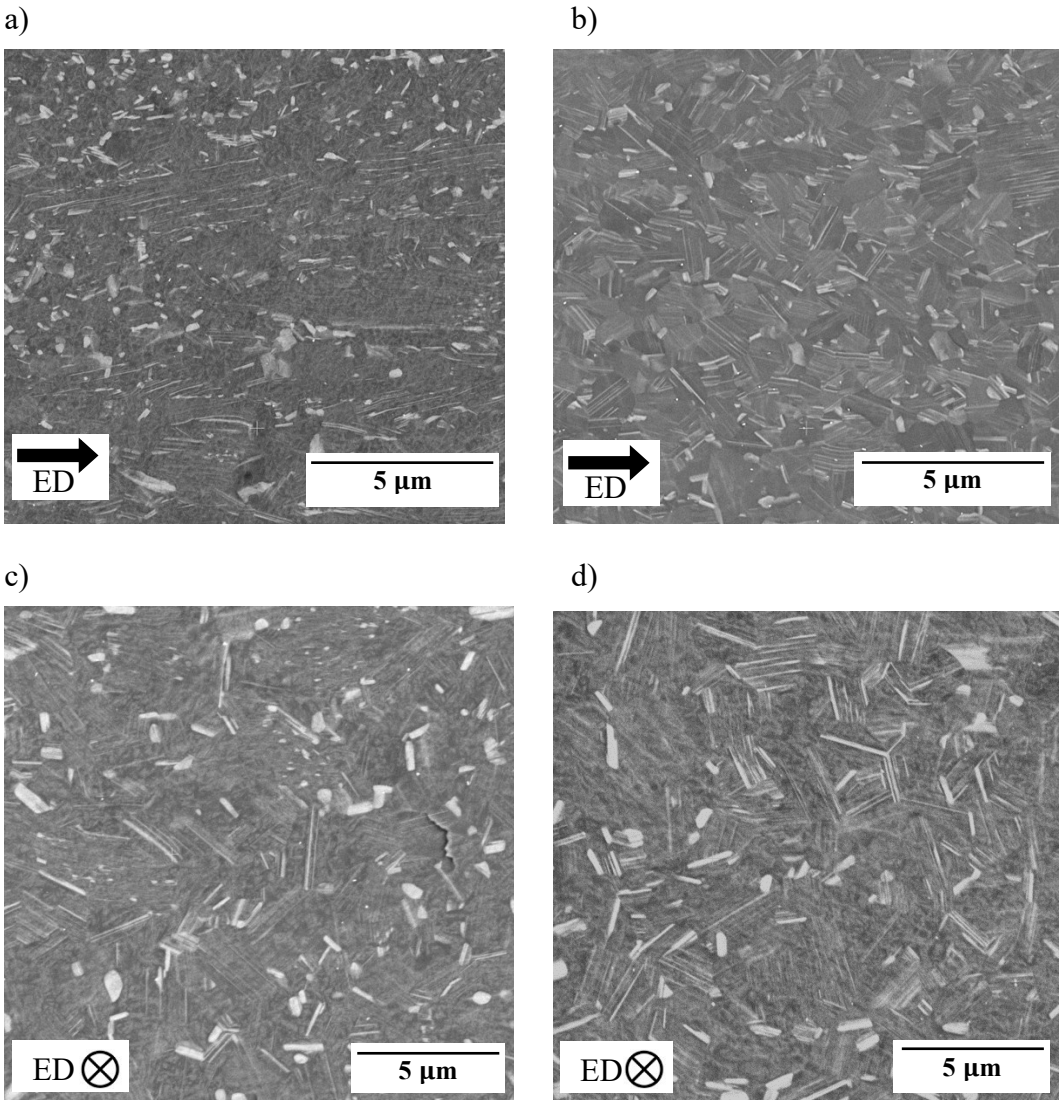

Figure 4.4. BSE images of the (a,c) RS 5.0 and (b,d) RS 6.7 samples in longitudinal and cross section, respectively.

The orientation EBSD maps for all investigated alloys are presented in Figures 4.5 - 4.6. Only the points with confidence index (CI) > 0.1 are shown, therefore the black areas correspond to the areas where the software cannot properly analyse the obtained Kikuchi diffraction patterns. In case of CE samples, these areas correspond to LPSO fractions visible in BSE images, Figure 4.3. In case of the RS samples, those areas are originated from the overlapping of diffraction patters from few small grains because of large penetration depth of electron beam interacting with these small grains. The average grain sizes of the investigated samples, determined with the OIM software, are presented in Table 4.1.

Table 4.1. Average grain size of the investigated alloys.

Extrusion ram speed	5.0 mm/s	6.7 mm/s
CE $Mg_{97.94}Zn_{0.56}Y_{1.5}$	8.8 $\pm$ 1.5 µm	9 $\pm$ 3 µm
RS $Mg_{97.94}Zn_{0.56}Y_{1.5}$	0.8 $\pm$ 0.2 µm	0.9 $\pm$ 0.2 µm

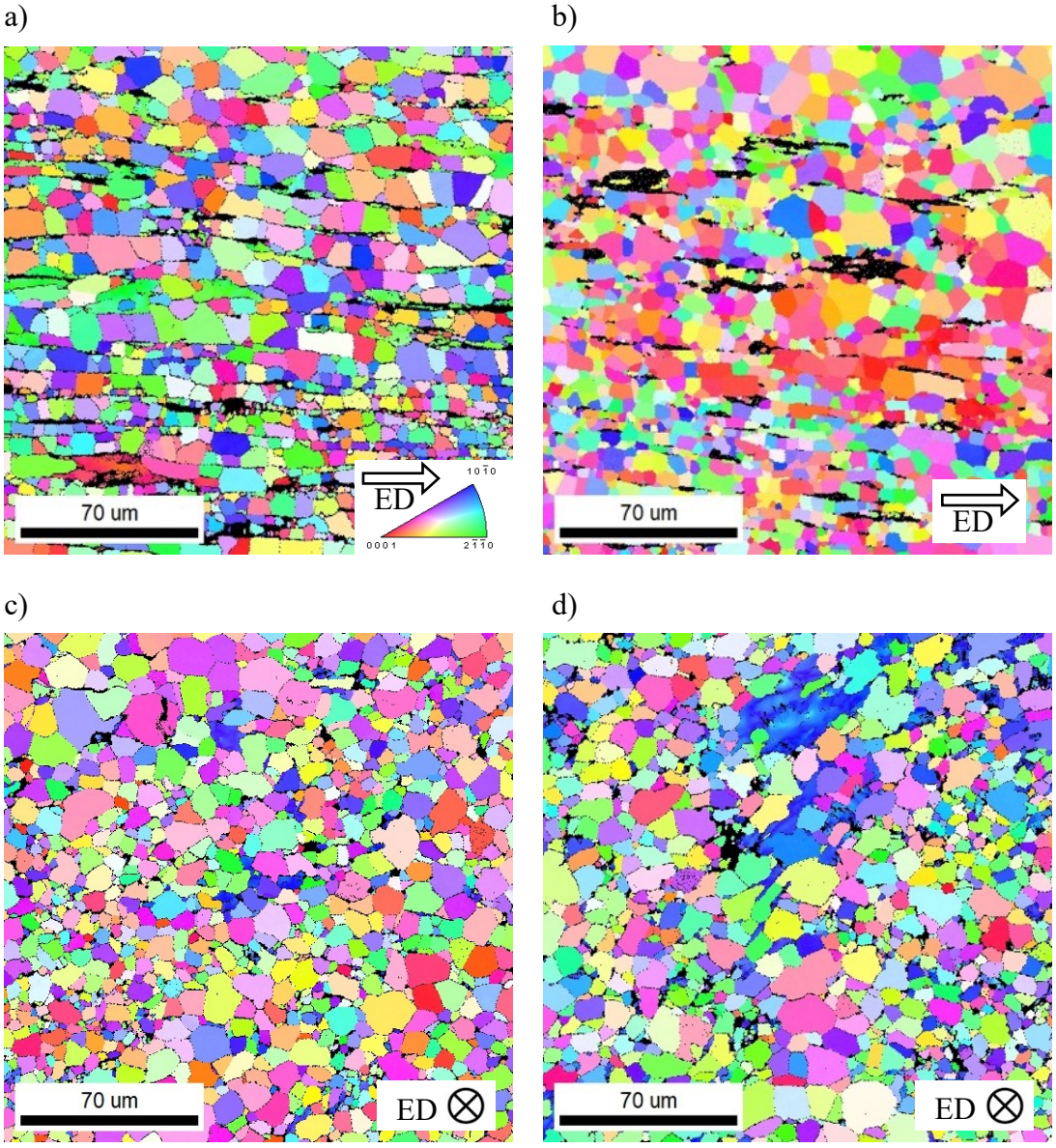

Figure 4.5. The orientation EBSD maps of the (a,c) CE 5.0 and (b,d) CE 6.7 samples in longitudinal and cross section, respectively.

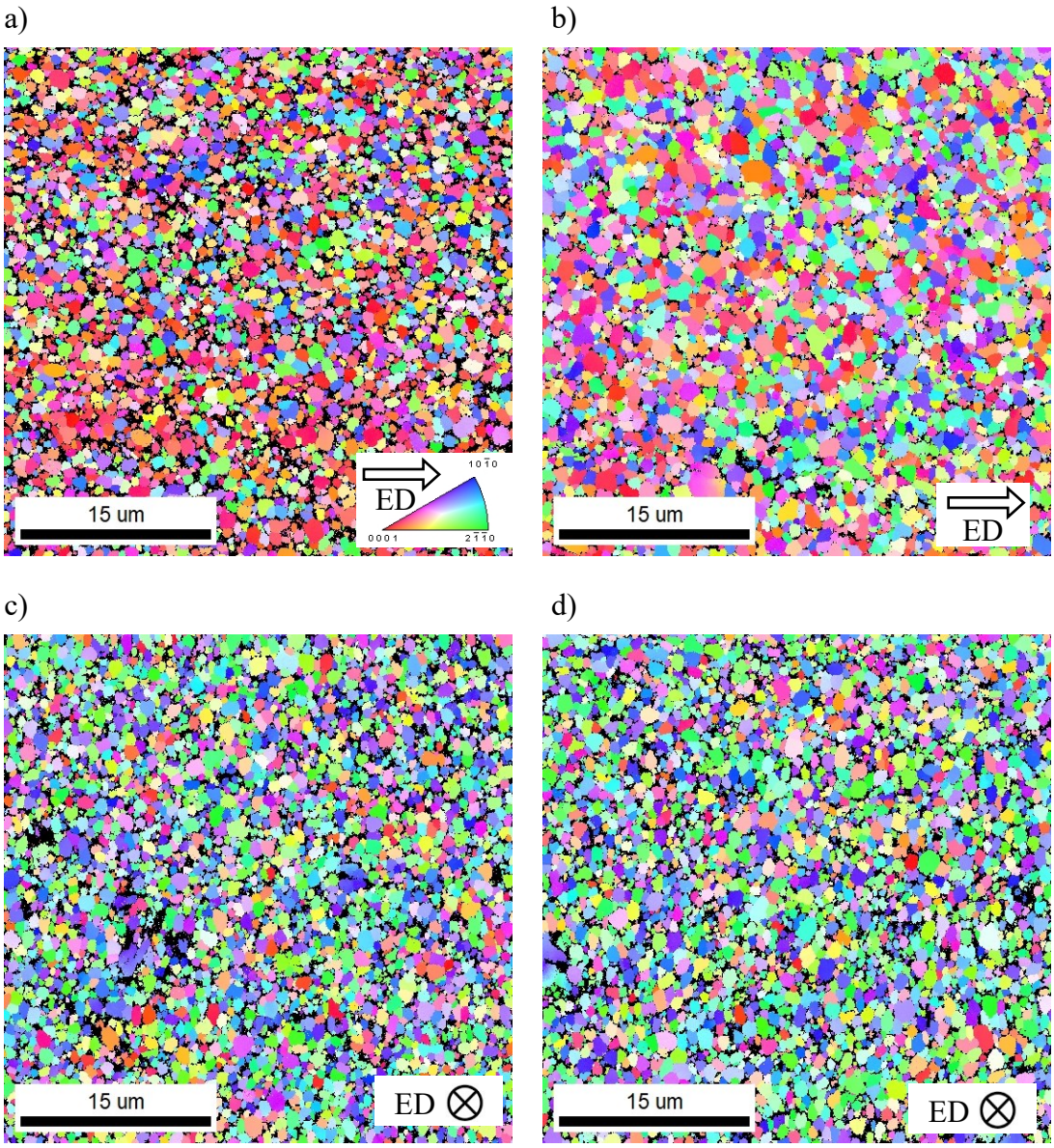

Figure 4.6. The orientation EBSD maps of the (a,c) RS 5.0 and (b,d) RS 6.7 samples in longitudinal and cross section, respectively.

Moreover, using obtained EBSD maps, the Schmid factors analysis has been performed, see Figure 4.7. The Schmid factors for the grains at the cross section was calculated using the program OIM. It is obvious that in the case of CE alloys (independently on extrusion speed), part of grains has favourable orientation for basal slip (red-coloured grains in first column). In contrary, both RS alloys are characterized by lower values of Schmid factor for basal slip (non-red coloured grains), while values for prismatic and pyramidal slip are rather close to maximum value (represented by red colour).

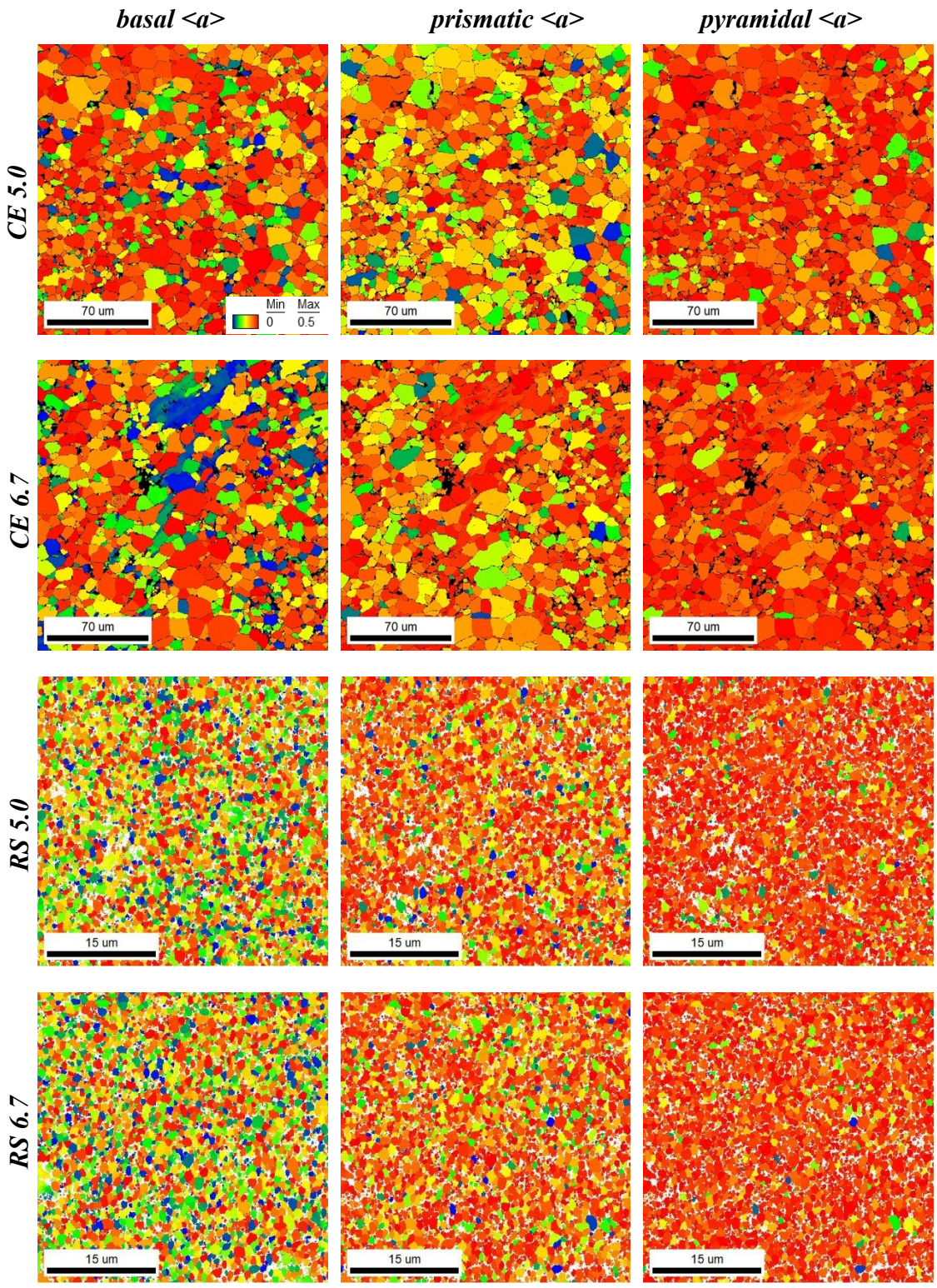

Figure 4.7. Schmid factor analysis for activation of the basal <a>-, prismatic <a>- and pyramidal <a>- slip systems for the CE 5.0, CE 6.7, RS 5.0 and RS 6.7 alloys. ED is perpendicular to image plane.

The texture of the investigated alloys recalculated from the X-ray diffraction data are presented in Figure 4.8. All materials are characterized by so-called basal texture with slightly higher intensity at [-1100] pole in the texture triangle. That means, that majority of the grains have their basal plane oriented nearly parallel to ED. However, the textures, independently on processing technique and extrusion ram speed, are rather weak, having a maximum intensity of approximately 1.7 m.r.d. (multiples of random density) for RS alloys and approximately 2 m.r.d. for the CE alloys.

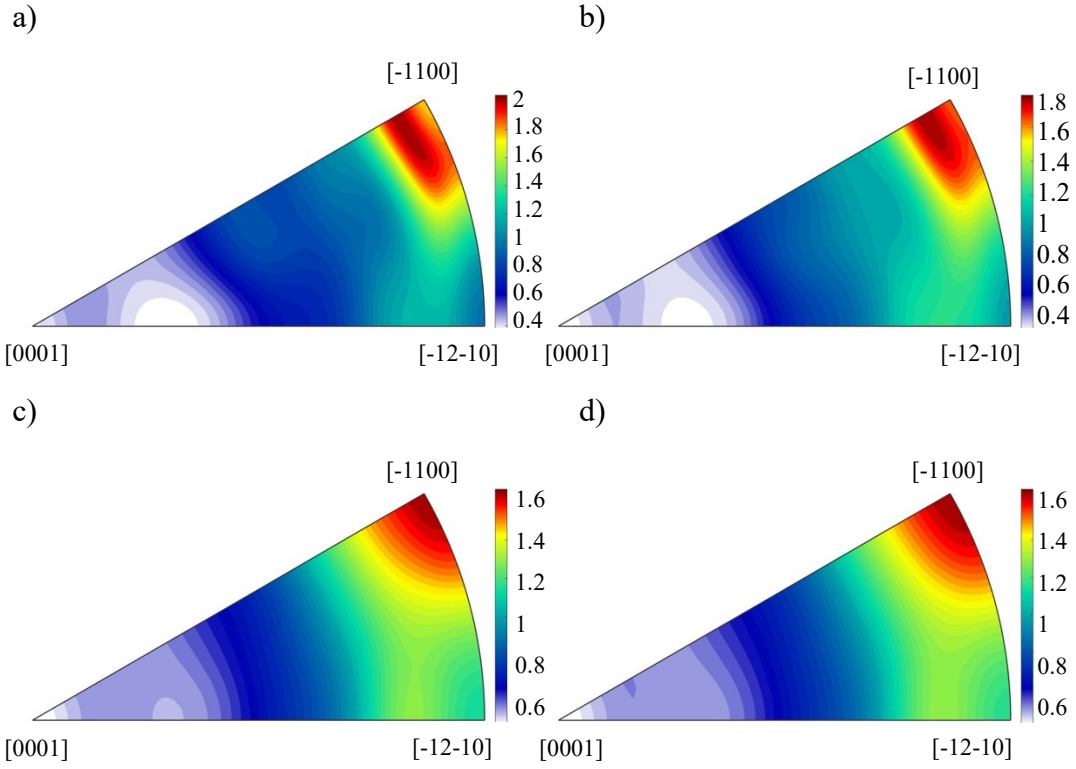

Figure 4.8. Texture triangles obtained by X-ray diffraction for the a) CE 5.0, b) CE 6.7; c) RS 5.0 and d) RS 6.7 alloys. ED is perpendicular to the image plane.

As another way of presenting texture, the intensity developments of the diffraction peaks as the function of azimuthal angle ψ at the beginning and at the end of the deformation tests are presented in Figure 4.9. The ψ angle represents the tilt from the loading direction (see Figure 3.2). Thus, the angle of 0° corresponds to the radial direction (perpendicular to ED) and 90° to the axial direction (along ED). Similarly to results presented in Figure 4.8, all four investigated alloys show a similar

texture, therefore texture in shape of angle distribution are presented only for RS 6.7 and CE 6.7 alloys: in the initial state in Figure 4.9 (a,c), and after tensile loading in Figure 4.9 (b,d). It is obvious, that there is no significant change in the texture during the deformation, as seen from Figure 4.9 (a,b) for CE 6.7 alloy and Figure 4.9 (c,d) in case of the RS 6.7 alloy.

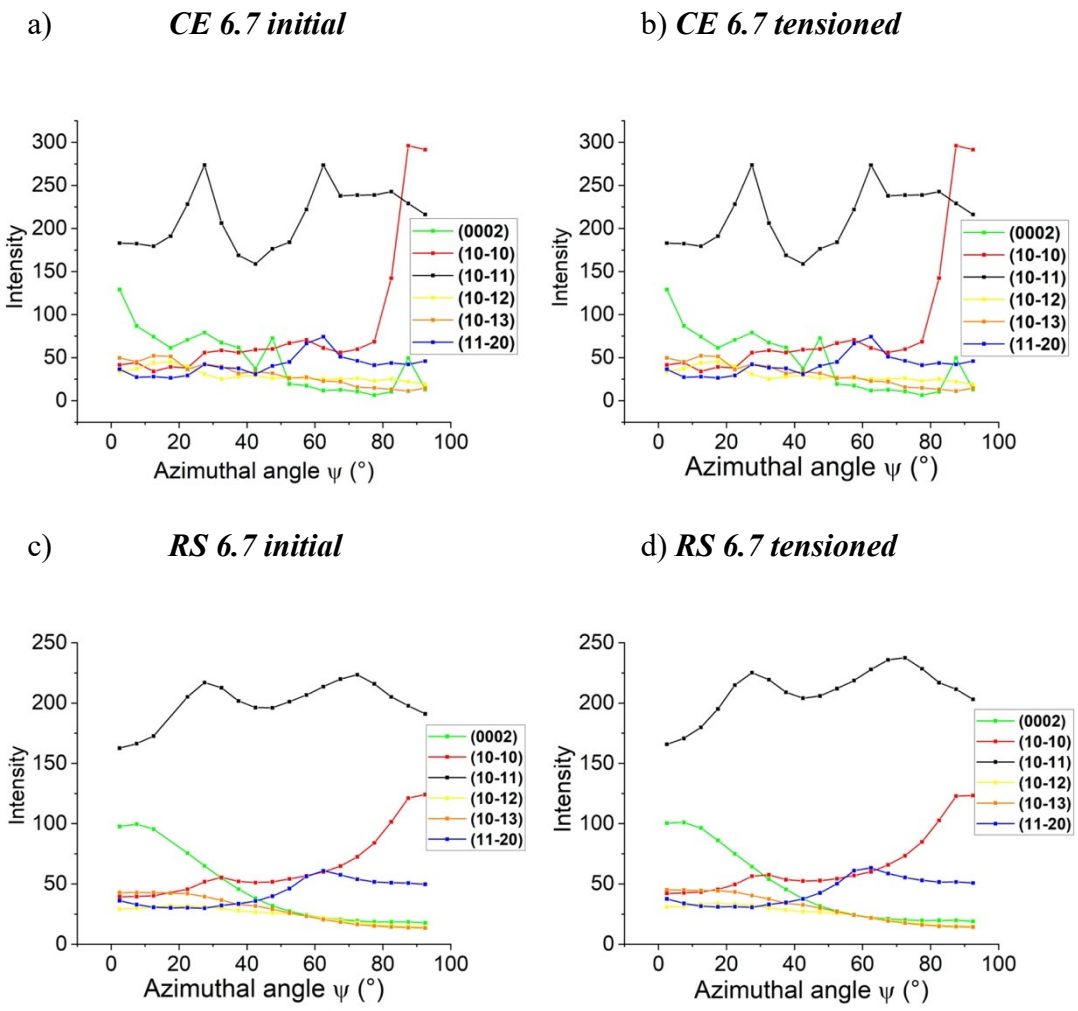

Figure 4.9. The intensity development of diffraction peaks as the function of the azimuthal angle ψ at the beginning (a,c) and at the end (b,d) of the tensile deformation tests for the (a,b) CE 6.7 and (c,d) RS 6.7 alloys.

The (0002) peaks intensity is concentrated in the radial direction (green line has high intensity at 0°) which indicates that the basal planes are oriented along ED. Its intensity decreases with increasing angle. The (10-10) prismatic planes intensity increases with increasing angle and have its maximum at the axial direction, which

means that the majority of the (10-10) planes is aligned perpendicular to the loading direction. The (10-11) diffraction peak has two maxima at 30° and 80° which corresponds to the first order pyramidal plane. The (11-20) peak is more homogeneously distributed comparing to (0002) and (10-10) planes with slightly higher values at approximately 65°. The (10-12) and (10-13) diffraction peaks are distributed homogenously with a slight decrease with increasing angle.

4.2. Mechanical properties

The mechanical properties of the investigated alloys have been revealed by uniaxial tensile and compression tests. The stress-strain curves are presented in Figure 4.10 and values of tensile and compression yield strength (TYS and CYS, respectively) and their difference ($\Delta = |\mathrm{TYS} - \mathrm{CYS}|$) are summarised in Table 4.2.

It is obvious, that RS alloys are characterized by high YS values in tension and compression (over 360 MPa and 400 MPa, respectively), which are significantly higher than TYS and CYS values for the CE alloys. Despite all investigated RS alloys show lower ductility compared to the CE alloys, the elongation to fracture of RS alloys still exceeds 10% of strain. In both types of processing (CE and RSRC) the higher extrusion ram speed led to better ductility, what is more significant for CE alloys.

All investigated alloys are characterized by higher CYS than TYS values, which is called a reverse tension-compression YS asymmetry (Table 4.2). However, this asymmetry is more significant in case of the RS alloys comparing to the CE alloys. Moreover, faster extrusion ram speed (6.7.mm/s) during RSRC processing leads to reducing this asymmetry.

The tensile curves of CE alloys have a convex shape, while compression curve is characterized by plateau after yielding and followed by hardening, i.e., so-called S-shape is observed, which usually indicates twinning activity. In the case of the RS alloys, after the linear elastic region the yield point (YP) phenomenon is observed during both, tension and compression loading. After reaching the upper YP a drop in the stress till the lower YP is present, which is followed by a plateau and necking leading to the fracture of the sample. Thus, the TYS for the RS alloys equals to the ultimate tensile strength (UTS). But in case of CE alloys, after reaching YS and

plateau, the strain hardening is following, therefore the ultimate compression strength is greater than the CYS values.

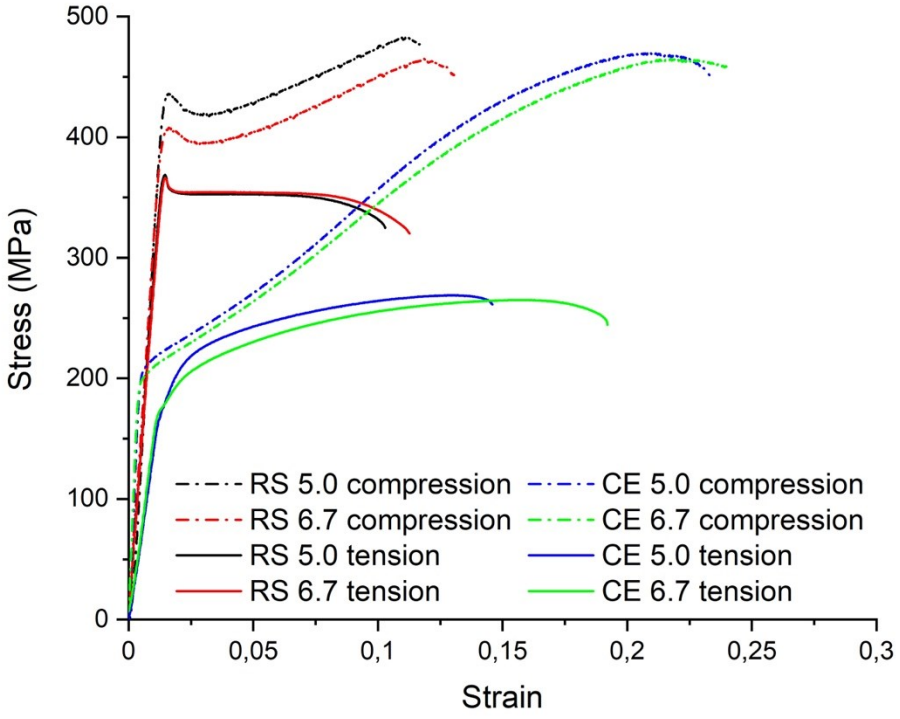

Figure 4.10. The strain-stress curves for the investigated RS and CE alloys.

Tab. 4.2. The YS values for the investigated alloys.

Alloy	TYS (MPa)	CYS (MPa)	Δ (MPa)
RS 5.0	369 ± 3	436 ± 3	67 ± 4
RS 6.7	366 ± 3	408 ± 3	42 ± 4
CE 5.0	182 ± 5	206 ± 5	24 ± 7
CE 6.7	178 ± 5	197 ± 5	19 ± 7

It is obvious that in case of RS alloys, the values of TYS are smaller than for CYS. Therefore, in order to improve TYS values, further investigations of the deformation mechanisms during tensile loading, including background processes leading to the YP phenomenon, are required.

4.3. Diffraction measurements

In order to obtain detailed insight into microstructure development and thus, active deformation mechanisms, the *in-situ* diffraction measurements were performed during tensile loading of RS alloys (both RS 5.0 and RS 6.7). Data for CE alloys (both, CE 5.0 and CE 6.7) are serving as a reference. The evolution of the lattice strain (LS) in the axial direction as a function of engineering strain and stress are presented with the deformation curves in Figures 4.11- 4.21.

In the case of CE alloys, the intensity of the (0002) plane in the axial direction is nearly zero (see also Figure 4.9), therefore it is difficult to fit this peak. Considering the evaluation error, the data related to this peak are not presented in the following graphs. The LS evolution as a function of strain for CE 5.0 (Figure 4.11) indicate that at the beginning of the loading, all LS follow a straight line. Then, still in macroscopically elastic region (cf. the corresponding deformation curve plotted in Fig. 4.11), LS of the (10-13) and (10-12) peaks start to deviate from main trend, slightly increasing in their values (note negative scale of the Y-axis) and shortly after yielding persist constant till the end of the test. The LS evolution for the (10-11) peak exhibits slight decrease in elastic part, followed by increasing till fracture. Similar tendency is present for the (11-20) peak, but deviation starts at higher applied load. The LS evolution for (10-10) does not show increase in values during the entire loading. In order to estimate the activation stress for individual mechanisms, the LS developments are also presented as a function of engineering stress (Figure 4.12). The linear response of the diffraction peaks in CE 5.0 is valid till approximately 150 MPa where the planes start to behave differently (Figure 4.12). Particularly, LSs of the (10-11), (10-12) and (10-13) planes deviate from the linear response to positive values, followed by constant character in case of the (10-11) and (10-12) peaks up to 240 MPa, and changing into decreasing from 240 MPa till the end of the test. LS of both the (10-10) and (11-20) peaks start to deviate to negative values at 150MPa, followed by symmetrical split deviation at 160 MPa: LS of the (10-10) peak continue to decrease during entire deformation test, while LS of the (11-20) peak remains constant from 170 MPa till 200 MPa and followed by the decrease in LS values. The CE 6.7 alloy is characterized by similar behaviour with more abrupt growth in the lattice strain at 175 MPa for the (10-11), (10-12) and (10-13) peaks, see Figures 4.13-14.

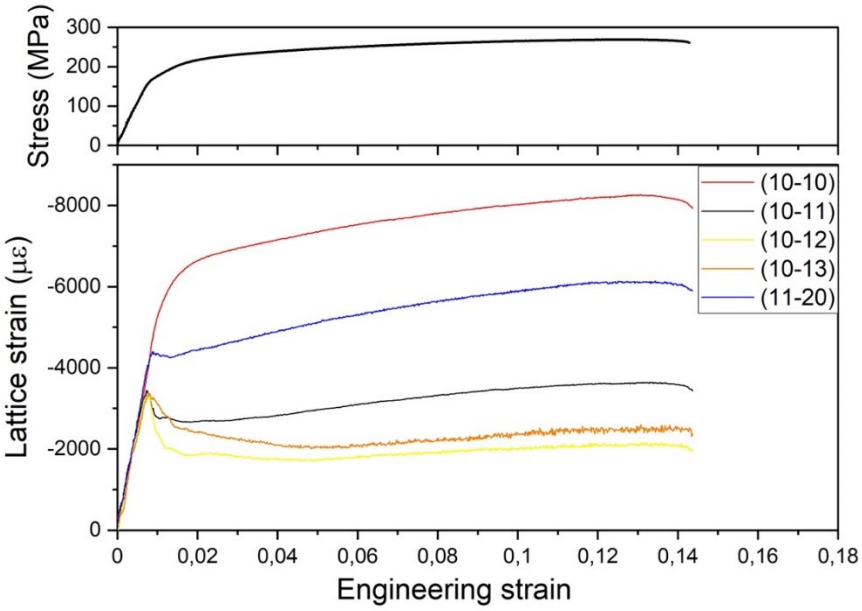

Figure 4.11. The macroscopic strain-stress curve and the axial lattice strains as a function of engineering strain for the CE 5.0 alloy.

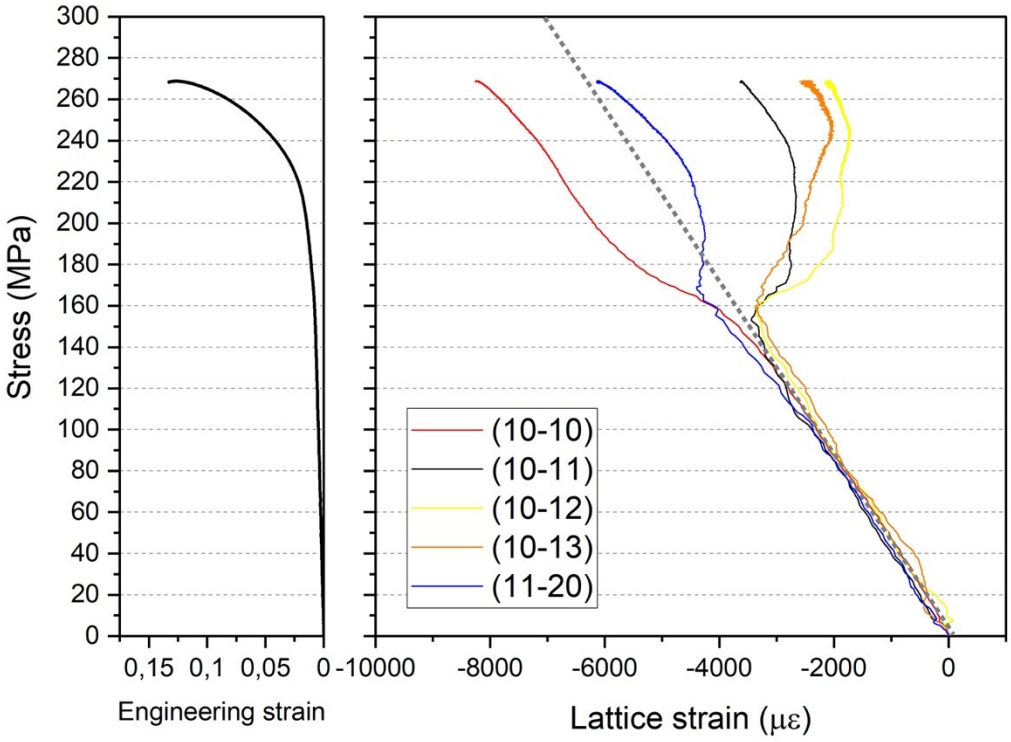

Figure 4.12. The macroscopic stress-strain curve and the axial lattice strains as a function of stress for the CE 5.0 alloy.

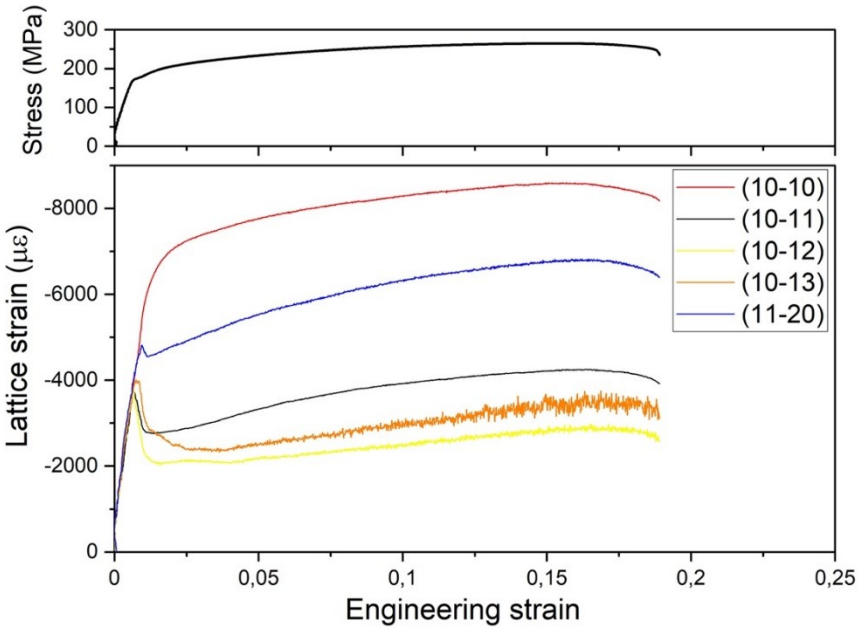

Figure 4.13. The macroscopic strain-stress curve and the axial lattice strains as a function of engineering strain for the CE 6.7 alloy.

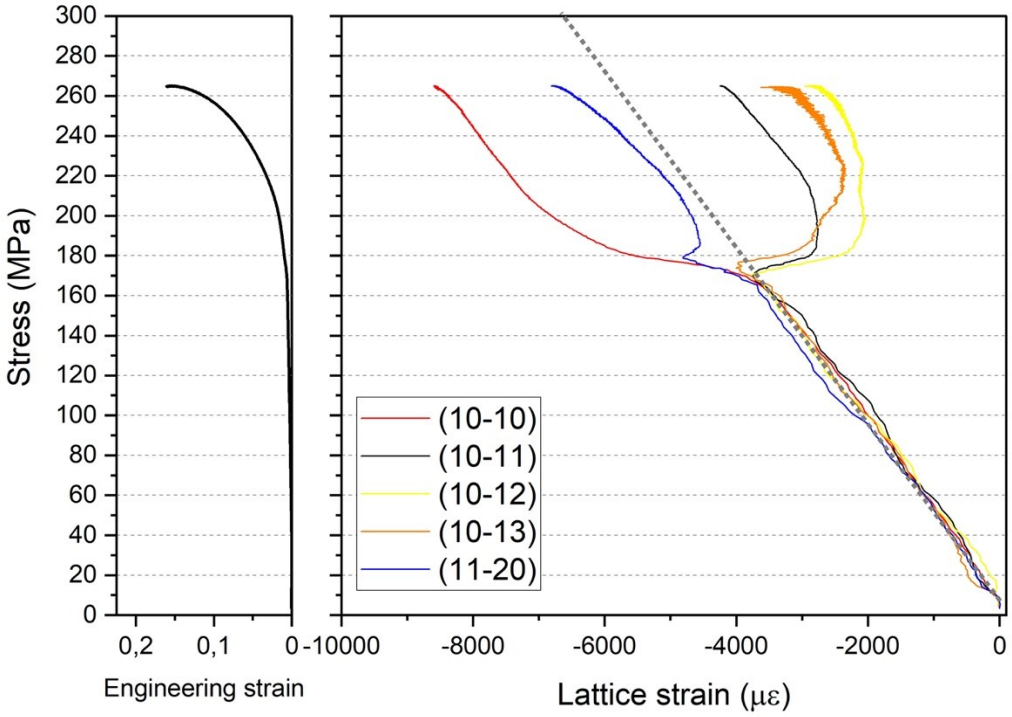

Figure 4.14. The macroscopic strain-stress curve and the axial lattice strains as a function of stress for the CE 6.7 material.

The results of the *in-situ* synchrotron diffraction measurements for the RS alloys are presented in Figures 4.15-18. Moreover, for better visibility the stress-LS curves zoomed at the YP area are depicted in Figure 4.19.

Figures 4.15 and 4.17 indicate that independently on extrusion speed, the LS evolutions for the RS alloys correspond to the macroscopic curves, i.e. LSs of all planes are characterized by a similar tendencies copying the shape of the macroscopic curve. The slight linear deviation of the LS for (0002) plane from the ideal elastic response from the beginning of the test (Figures 4.16 and 4.18) can be explained by low intensity and higher evaluation error comparing to that for LS of other peaks. (The LS evolution of (10-11) peak is not presented for RS 6.7 because of the high error in fitting.) The LS evolution plotted against macroscopic strain (Figures 4.15 and 4.17) with a closer look around YP (enlarged images in Figures 4.15 and 4.17) indicate that all of the planes are showing a decrease in LS till the upper YP (369 MPa for RS 5.0 and 366 MPa for RS 6.7), after an increase in the LS values takes place till the lower YP (352 MPa for RS 5.0 and 354 MPa for RS 6.7) than an abrupt gain in LS is followed by slight increase till the fracture.

In contrast, the LS evolutions depicted as a function of stress, including enlarged view in Figure 4.19, present detailed development of LS in the close proximity to YP. Particularly, in case of RS 5.0, the LS evolutions of the (0002), (11-10), (10-10) and (10-13) peaks (green, blue, red, orange lines, respectively) continue to decrease during yielding reaching upper YP, and only after start to deviate to positive values with decreasing in applied stress till lower YP. At the same time, LS for the (10-11) and (10-12) peaks start to deviate into positive values already before upper YP (~ 357 MPa) and continue to increase with applied stress till lower YP.

In case of RS 6.7 alloy, the LS evolutions of the (0002), (11-10), (10-10) and (10-13) peaks (green, blue, red, orange lines, respectively) are characterized by similar tendencies as in the RS 5.0 alloy. However, there is no deviation of LS for the (10-12) peak (yellow line) from the ideal elastic response.

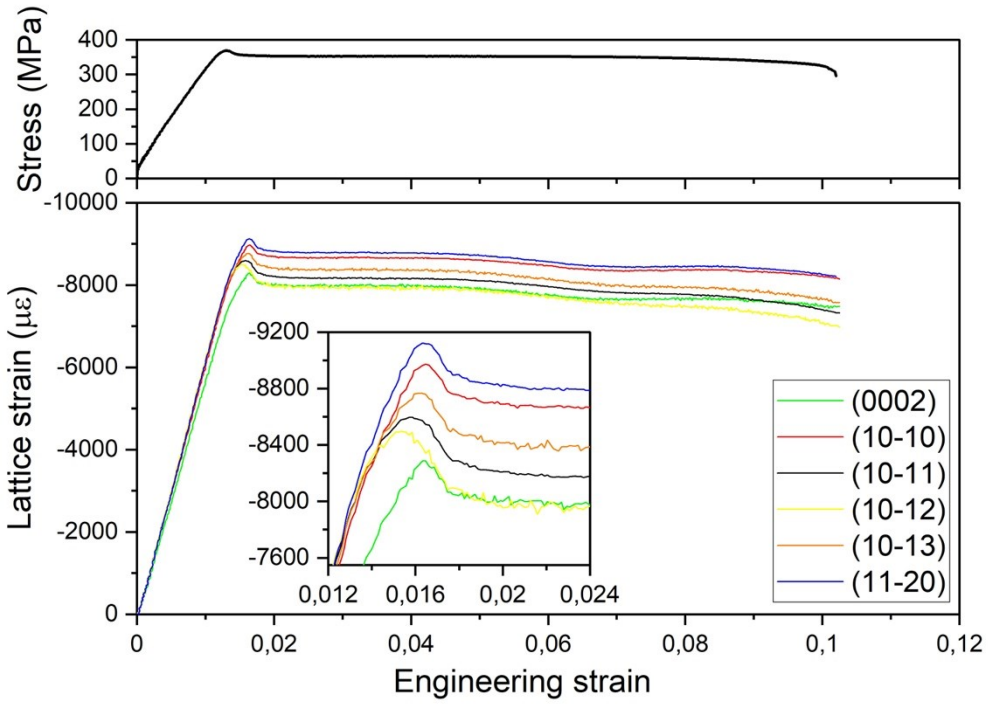

Figure 4.15. The macroscopic strain-stress curve and the axial lattice strains as a function of engineering strain for the RS 5.0 alloy.

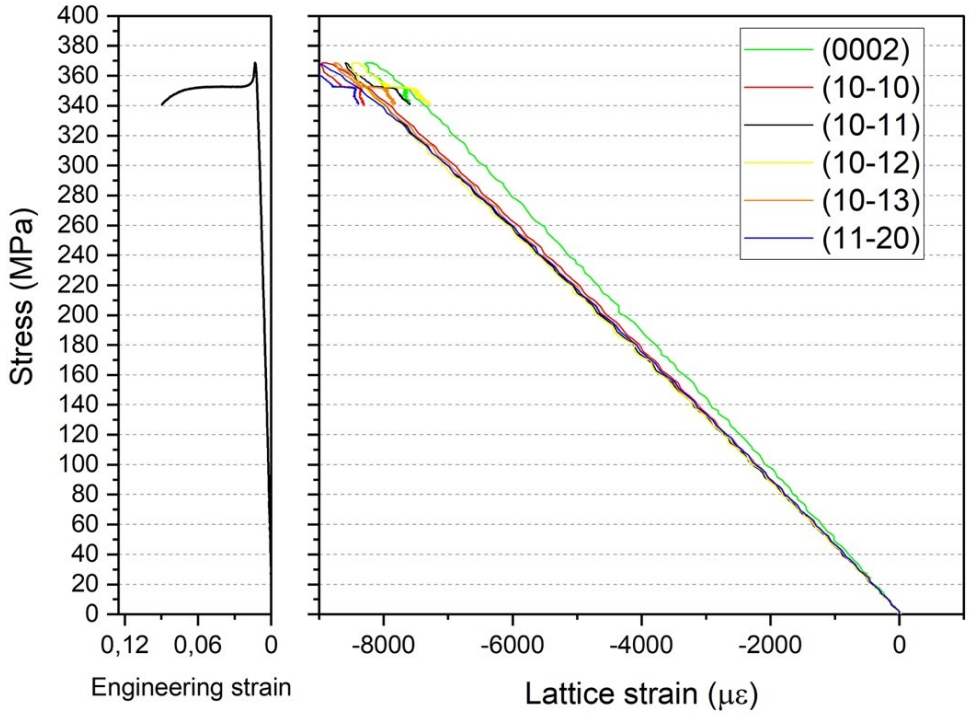

Figure 4.16. The macroscopic strain-stress curve and the axial lattice strains as a function of stress for the RS 5.0 alloy.

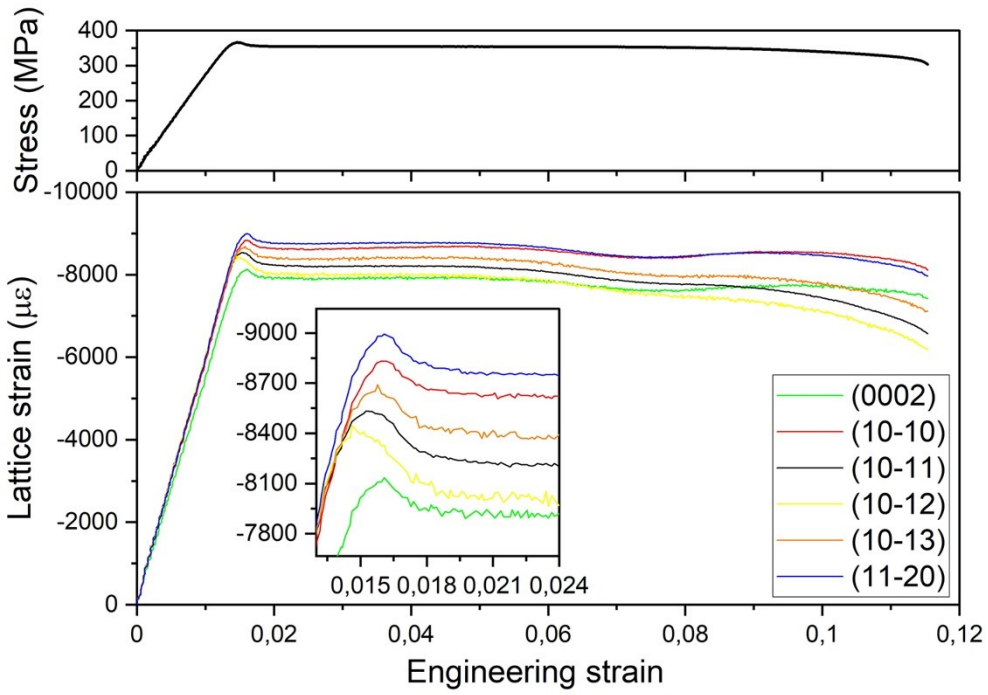

Figure 4.17. The macroscopic strain-stress curve and the axial lattice strains as a function of engineering strain for the RS 6.7 alloy.

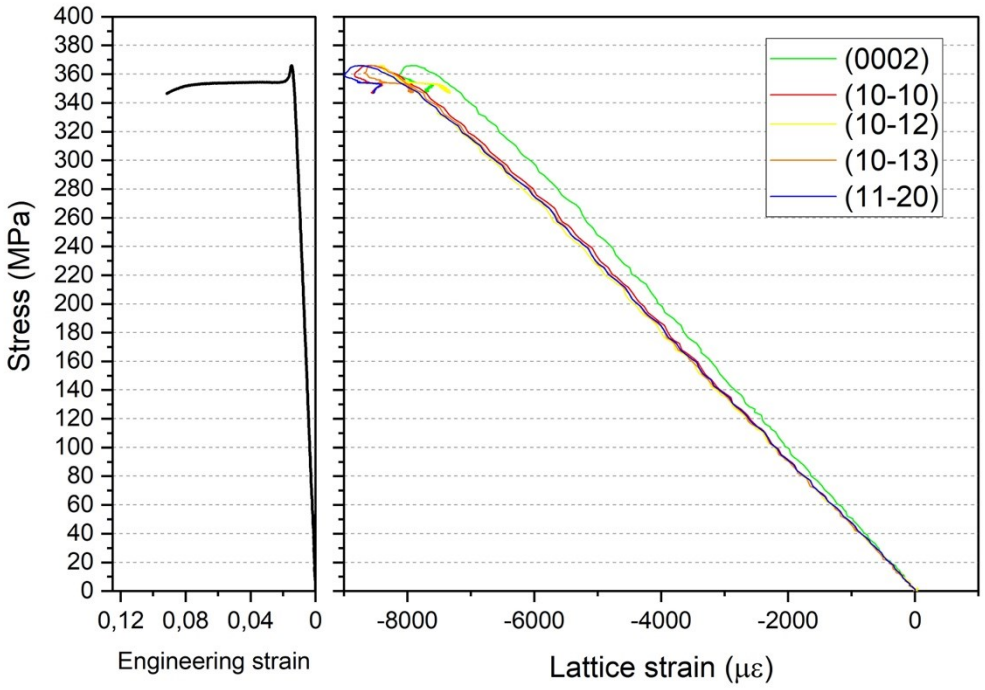

Figure 4.18. The macroscopic strain-stress curve and the axial lattice strains as a function of stress for the RS 6.7 alloy.

a)

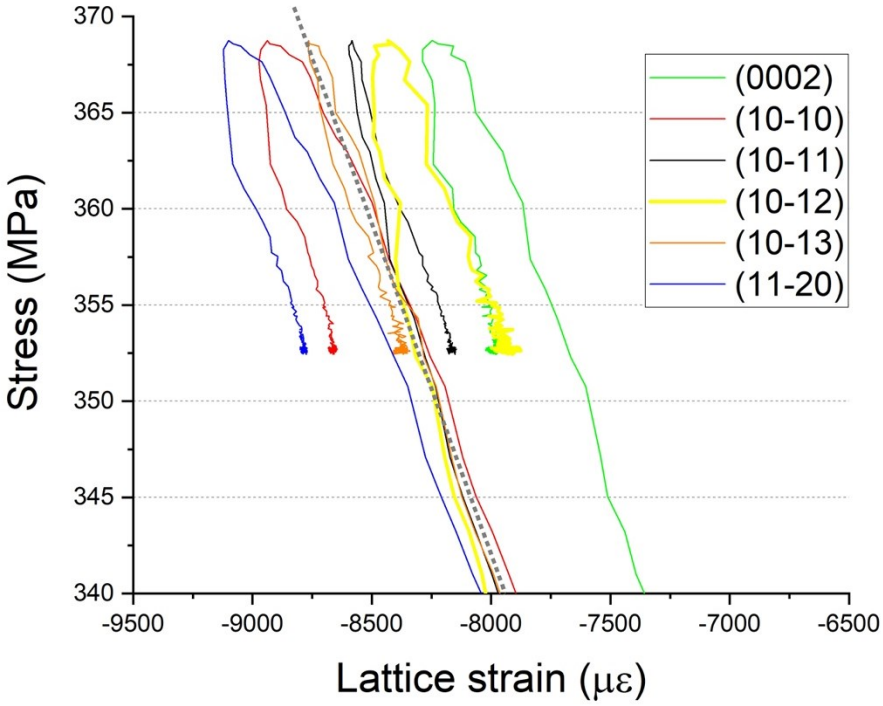

b)

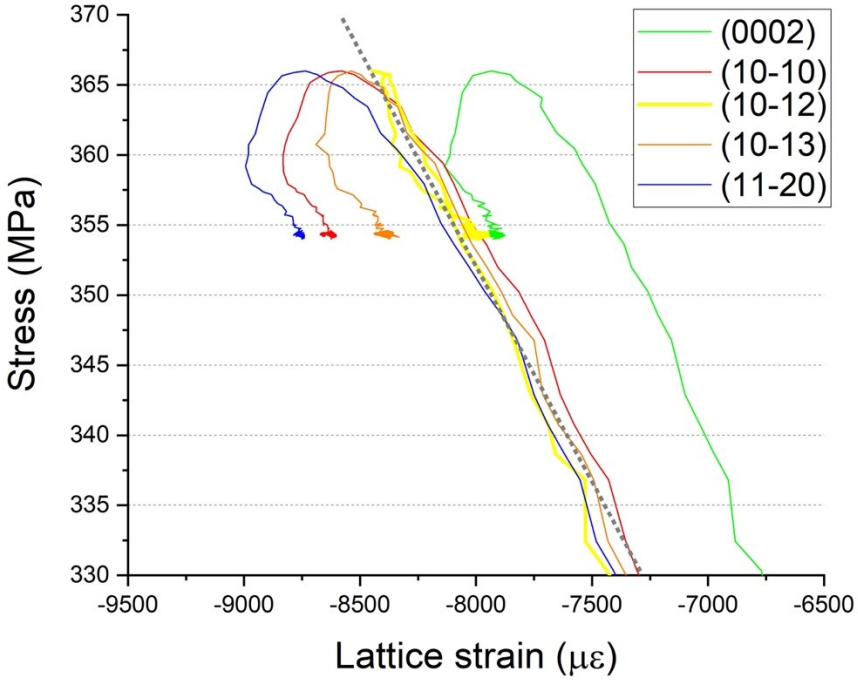

Figure 4.19. The axial lattice strains as a function of stress zoomed at the YP area up to achieved strain of 0.04 for the a) RS 5.0 and b) RS 6.7 alloys.

The evolution of the relative intensity of the diffraction peaks (the integrated intensity divided by the background) in the axial direction with the macroscopic loading as a function of time is shown in Figures 4.20 and 4.21 for the RS 5.0 and RS 6.7 alloys, respectively. The macroscopic data nicely corelates with the microscopic diffraction data. In the case of the RS 5.0 sample, it can be seen, that the basal plane (0002) is decreasing till upper YP, where it has a minimum and starts to increase afterwards. The same is the situation with the (10-12) and (10-13) diffraction peaks. The prismatic plane (10-10) is decreasing till the lower YP, and after it has a virtually constant value. The intensity for (11-20) peak is almost constant with a slight increase before necking and final fracture. The intensity of the (10-11) peak shows a gradual increase during the whole deformation with a rapid jump at YP. In the case of the RS 6.7 alloy similar trends can be observed but the intensity development of the (0002) diffraction peak is not so significant. The same drop of intensity at YP is present for the (10-10), (10-12) and (11-20) peaks with a following increase in its values. The same trend is also present for the intensity of the (10-11) plane.

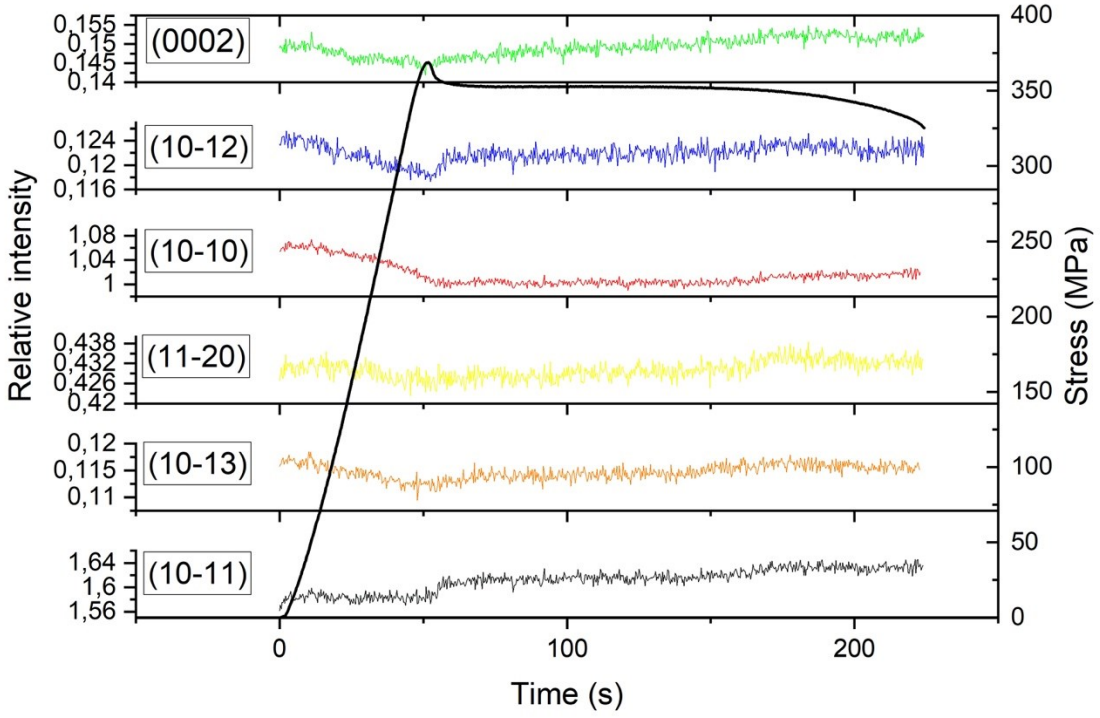

Figure 4.20. The relative intensity development of the diffraction peaks with the macroscopic loading as a function of time for the RS 5.0 alloy.

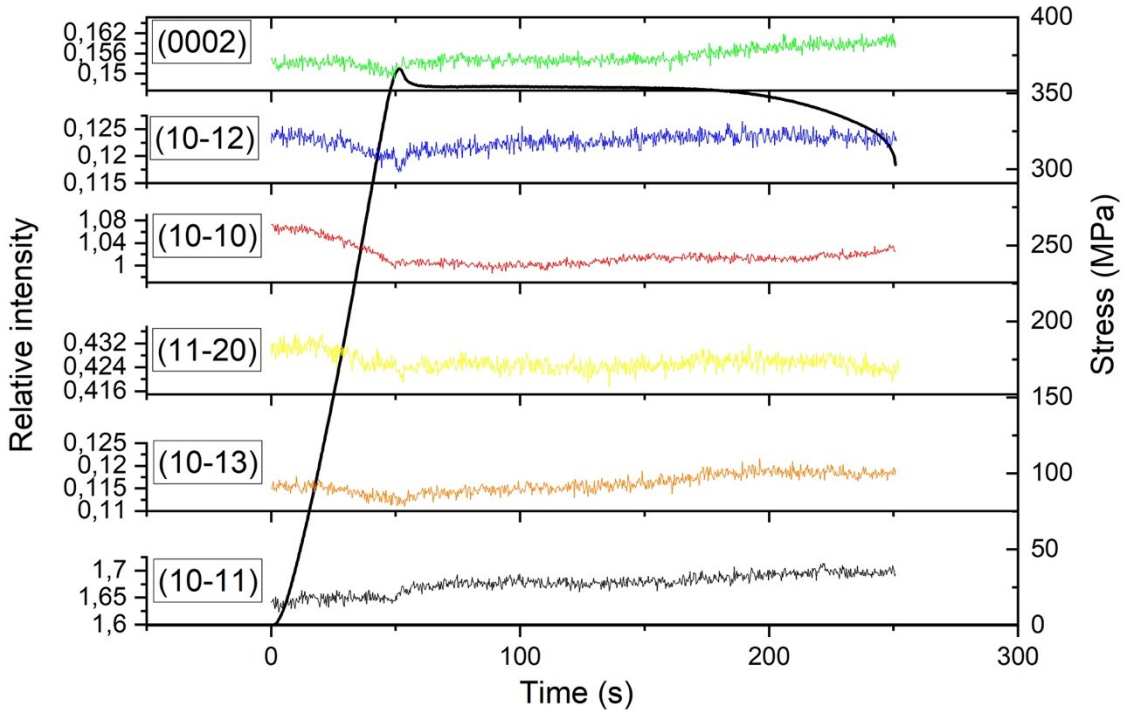

Figure 4.21. The relative intensity development of the diffraction peaks with the macroscopic loading as a function of time for the RS 6.7 alloy.

5. Discussion

It is obvious that the RSRC technique leads to the formation of microstructure with significantly smaller grains comparing to that of CE alloys. In general, the RS alloys are characterized by approximately 10 times smaller average grain size compared to that for the CE alloys (see Tab. 4.1). Despite of the large uncertainty in the obtained values, within errors the results for the RS alloys correspond to the data reported in [17]. It can be also seen that slightly faster extrusion ram speed yields slight increase in grain sizes. Moreover, type of the processing technique has a significant effect on the formation of the LPSO phase and/or solute segregated SFs or CALs. Particularly, both CE alloys, independently on extrusion speed, are characterized by presence of LPSO phase, while there are no LPSO fractions observed in the RS alloys. Instead, more homogeneous distribution of the alloying elements in forms of solute segregated SFs and/or CALs dispersedly distributed in the grain interior are observed in materials processed by RSRC technique.

Moreover, the RSRC method results a rather weak basal texture having higher intensity at the [-1100] pole in the inverse pole figure [26]. The formation of basal texture is caused by the lattice rotation due to non-basal slip with the <11-20> direction during extrusion [27]. The maxima of texture intensities are lower in the case of RS materials compared to the CE alloys, despite all investigated alloys are characterized by weak texture comparing to conventional Mg alloys [2]. In general, the fine DRX grains have a random orientation and preferential orientation of the non-DRX grains are contributing to the higher intensity at the [-1100] pole [16]. The coarse non-DRX grains elongated along ED can be seen in Figure 4.2. Figure 4.9 shows high intensity at 0° for the (0002) plane, which indicates alignment of the basal planes with ED. The (10-11) plane has two maxima at approximately 30°and 80°, which can be explained by the angle between the two prisms of the hexagonal structure. It can be can also concluded, that there is no twinning during the tensile deformation, because the same intensity trends are visible at the beginning and also at the end of the tests for every plane (Figure 4.9).

From the deformation tests it can be clearly seen that the RS alloys have a higher yield strength with values over 365 MPa given by homogeneous distribution of the solute segregated SFs and CALs. The CE alloys have better ductility. Moreover, the alloys produced with extrusion ram speed of 5.0 mm/s, have worst ductility

compared to the faster processing (extrusion ram speed is 6.7 mm/s), although in the strength the difference is not that conspicuous.

From engineering point of view, the best materials are the ones with the smallest difference in the TYS and CYS values. From Figure 4.10 it is obvious that the RS 5.0 alloy have better compression resistance, but therefore a greater difference (Δ) between TYS and CYS. Thus, the RS 6.7 alloy even having a slightly lower YP during tensile and compression loading, is a better candidate because of the approximately 25 MPa smaller value in the discussed difference. In the case of the CE alloys the difference between the YSs is relatively minor. Also, identifying the YP for the CE alloys was more challenging compared to the RS alloys, as there was no sharp value, but rather a continuous transition from elastic to plastic behaviour.

The foremost sight which captures attention in the case of compression loading of the CE alloys is the S-shaped curve, which indicates twinning activity. The reason for the operation of this mechanism is suitable texture with respect to loading axis: as majority of the grains have their c-axis perpendicular to loading direction, the extension twinning can be easily activated [14]. Moreover, basal slip system is operating in well oriented grains, and also non-basal slip systems are activated when sufficient stress is achieved. Kinking mechanisms is likely suppressed due to low fraction of LPSO given by low amount of alloying elements. The compression deformation behaviour is in good agreement with results reported in [28].

The deformation mechanisms during tension of the CE alloys were investigated in more detail using *in-situ* X-ray diffraction technique. Generally, the plastic deformation is related to the loss of elastic response in the lattice strain. In the case of the CE alloys, LSs of the (10-12), (10-13) peaks start to deviate to the right from the linear trend at 160 MPa for the CE 5.0 and at 170 MPa for the CE 6.7 alloy which is before the macroscopic yielding. Since both planes have high Schmid factor for the basal slip (0.43 and 0.39, respectively), the observed effect can be explained by the activation of basal <a>-slip. Moreover, in the case of the (10-12) plane the contribution of the pyramidal <a>-slip also cannot be excluded (SF=0.38). LS of the (10-11) planes also deviates at the same stress value, and it can be explained by the activation of pyramidal <a> dislocation slip (SF=0.47). LS of the (11-20) planes also deviate from the linear trend to the right, but it takes place later, at approximately 170 MPa for the CE 5.0 alloy and 180 MPa for the CE 6.7 alloy. This deviation is probably caused by

the activation of pyramidal <c+a>-slip system which has a highest Schmid factor (SF=0.45). LS of the (10-10) planes is deviating to the left from the linear response due to activity of the prismatic <a>-slip system with highest Schmid factor (SF=0.43). The activation of non-basal slip systems could improve ductile properties [29]. It should be noted that twinning activity was not present during tensile loading of CE alloys, since there are no different trends between the (0002) and (10-10) planes. When twinning happens, these peaks intensities would show different trends, because 86.4° rotation would change the diffraction conditions.

In RS alloys, the twinning activity is supressed in both tension and compression of the RS alloys due to small grains size given by the processing technique. Since the non-DRX coarse grains have their basal plane along ED, the Schmid factor for this plane is 0 therefore non-basal slip systems are activated in these grains during both tension and compression. At the same time, random orientation of the DRX grains enabling realization of several deformation mechanisms in variously oriented grains, contributes to moderate ductility [7]. However, the Schmid factor analysis (Figure 4.7) indicates that orientations of the grains are not preferable for basal slip. Therefore, non-basal slip (prismatic and pyramidal) should be activated, which requires higher applied stress due to high values of CRSS. Together with suppression of twinning, activation of non-basal slip leads to achieving high yield strength (in both compression and tension). Moreover, the dispersed SFs and CALs, being obstacles for dislocation movement, provide additional strengthening to the material.

Moreover, in the RS alloys the YP phenomenon occurs, which is a sudden drop in the stress after reaching the upper YP followed by the hardening of the material. The origin of this effect has been partly described in [30]: after reaching a certain external load the pinned dislocations by the segregated solute particles suddenly release, which indicates a drop in the strength values from upper YP to lower YP. In present work, the observed change in the diffracted intensity at the vicinity of the YP implies the rotation of the planes. These rotations are the product of the activation of slip systems, specifically the prismatic <a> in the (10-10), (11-20) planes, pyramidal <a> in the (10-11), (10-10), basal in the (10-12), (10-13) planes and also pyramidal <c+a> in the (0002) and (11-20) planes, which probably also causes the rotation of the basal planes at later stage of the deformation and a slight increase in intensity. The development of LS with respect to stress (Figure 4.19) indicate that the (0002), (10-

10), (11-20) and (10-13) peaks have a linear response till the upper YP, where the loss of elastic response implies the activation of pyramidal <c+a>-, prismatic <a>-, prismatic <a>- and pyramidal <c+a>-slip systems, respectively. For the (10-10) plane also the activation of the pyramidal <a>-slip system cannot be excluded. Same stands for the (10-13) plane and the basal slip. From the graph it can be also clearly seen that the black and yellow line- the (10-11) and (10-12) planes- are deviating to the right from the linear elastic response before achieving the upper YP at approximately 357 MPa, which implies the activation of pyramidal <a>- and basal slip system, respectively Therefore, the asynchronous transition between individual slip systems is supposed to be the reason of the YP phenomenon.

6. Conclusions

A bimodal character at the RS alloys with non-DRX grains elongated along ED and fine DRX grains with average grain size smaller than 1 μm has been revealed using the combination of light microscope and SEM. The CE alloys are characterized by homogeneous microstructure with an average grain size of about 9 μm. Moreover, the RSRC technique led to formation of solute-enriched SFs and CALs in the grain interior instead of complete LPSO phase at the grain boundaries in case of CE alloys. For all alloys, a weak basal texture is present with the basal planes oriented parallel to the ED. The tensile deformation tests showed the macroscopic mechanical properties of the alloys: the CE alloys have better ductility, but moderate strength compared to the RS alloys with high TYS over 365 MPa. A reverse tension-compression yield strength asymmetry is present in all alloys. For the RS 6.7 alloy, a smaller difference in the yield strengths has been observed comparing to that in RS 5.0, therefore it is more perspective for technical applications. For the RS alloys, the YP phenomenon has been revealed in both tension and compression tests. Deformation during compression of RS alloys is solely dislocation mediated and realized by basal and non-basal slip. The tensile deformations have been investigated using *in-situ* synchrotron diffraction technique. In the case of the CE alloys, before the macroscopic YS, first the basal <a>- and the pyramidal <a>-slip is activated on the (10-12), (10-13) and (10-11) planes. Later, the plastic deformation most likely proceeds with the activation of pyramidal <c+a>-slip system on the (11-20) planes. For the RS alloys, shortly before the macroscopic yielding the dislocation formation takes place. Slip systems are activated causing a change in the diffracted intensity. The most apparent change is at the (10-10) peaks intensity which is caused by the activation of prismatic <a>- and pyramidal <a>-slip systems.

Future perspective

Obtained data show evidence that the RSRC alloys have promising potential for widespread applications as structural material for engineering and biocompatible material for implantology. Despite the progress of the performed analysis, there are still unresolved questions regarding the behaviour of the alloys. To support findings addressed in present work and broaden related knowledge, the obtained results should be confirmed by transmission electron microscopy (TEM). Moreover, the experimental results could be also systematically compared with theoretical models. To better understand the unique YP phenomenon in relation to the alloys having fine-grained microstructure with solute segregated SFs it is essential to compare our experimental results with existing models or develop a new one with better description.

Bibliography

[1] Mordike, B.L., Ebert, T. Magnesium Properties - applications – potential (2001) Materials Science and Engineering A, 302 (1), pp. 37-45.

[2] K.U. Kainer, Magnesium Alloys and their Applications, Wiley-VCH Verlag GmbH, Weinheim, 2000.

[3] Railsback, L. Bruce. Abundance and form of the most abundant elements in Earth's continental crust (PDF). Some Fundamentals of Mineralogy and Geochemistry. (cited: 01.03.2024)

[4] M.M. Avedesian, H. Baker. Magnesium and Magnesium Alloys. The Materials Information Society, 1999.

[5] D. Drozdenko, et. al., The microstructure and anisotropic deformation behaviour of rapidly soldified ribbon consolidated Mg-Zn-X (X=Y, Gd, Nd) alloys. Journal of Alloys and Compounds. 944 (2023) 169175

[6] Y. Kawamura, K. Hayashi, A. Inoue, T. Masumoto, Rapidly Solidified Powder Metallurgy Mg97Zn1Y2 Alloys with Excellent Tensile Yield Strength above 600 MPa, Mater. Trans. 42 (2001) 1172–1176.

[7] M. Yamasaki, K. Hashimoto, K. Hagihara, Y. Kawamura, Effect of multimodal microstructure evolution on mechanical properties of Mg–Zn–Y extruded alloy, Acta Mater. 59 (2011) 3646–3658.

[8] K. Horváth, Doctoral thesis: Study of advanced high strength magnesium alloys by *in-situ* techniques, MFF UK, 2019

[9] G. Farkas, Doctoral thesis: Investigation of residual stresses and deformation mechanisms of magnesium-based composites by means of neutron diffraction and acoustic emission methods, MFF UK, 2017

[10] Hull, D. and D.J. Bacon. Chapter 1 - Defects in Crystals. In: D. Hull and D. J. Bacon, eds. Introduction to Dislocations (Fifth Edition). Oxford: Butterworth-Heinemann, 2011, pp. 1–20.

[11] Yoo, M.H. Slip, twinning, and fracture in hexagonal close-packed metals. Metallurgical Transactions A. 1981, vol. 12, no. 3, pp. 409–418.

[12] M.H. Yoo. Slip, twinning, and fracture in hexagonal close-packed metals, Metall Trans A 12 (1981) 409-418.

[13] R. von Mises, Mechanik der plastischen Formanderung von Kristallen, Z. Angew. Math Mech 8 (1928) 161-185.

[14] M.R. Barnett. Twinning and the ductility of magnesium alloys Part I: "Tension" twins, Mat Sci Eng a-Struct 464 (2007) 1-7.
[15] Schmid, E. And G. Wassermann. Über die Textur gezogener Magnesium- und Zinkdrähte. Naturwissenschaften. 1929, vol. 17, no. 18, pp. 312-314.
[16] G. Garces, P. Perez, S. Cabeza, H.K. Lin, S. Kim, W. Gan, P. Adeva, Reverse tension/compression asymmetry of a Mg-Y-Zn alloys containing LPSO phases, Mater. Sci. Eng.: A 647 (2015) 297-293.
[17] D. Drozdenko, M. Yamasaki, K. Máthis, P. Dobroň, P. Lukáč, N. Kizu, S.-i. Inoue, Y. Kawamura: Optimization of mechanical properties of dilute Mg-Zn-Y alloys prepared by rapid solidification, Materials & Design 181 (2019) 107984.
[18] K. Fekete, et. al., Thermal stability of the microstructure of rapidly solidified ribbon-consolidated $Mg_{97.94}Zn_{0.56}Y_{1.5}$ alloy, Material Characterization, Vol. 183 (2022) 111618.
[19] S. Ishizaki, et. al., Relationship between cluster-arranged nanoplate formation and mechanical properties of dilute- Mg-Zn-Y alloys prepared by combination of low-cooling-rate solidification and extrusion techniques, Matertrans., (2023) 1347-5320.
[20] M. Yamasaki, S. Izumi, Y. Kawamura, Development of high strength and highly corrosion-resistant bult nanocrystalline Mg-Zn-Y alloys with long period stacking ordered phase, ECS Trans. 16 (32) (2009) 81-88.
[21] MTEX. Available from https://mtex-toolbox.github.io (cited: 05.04.2024).
[22] Čapek, J. Investigation of basic deformation mechanisms of magnesium alloys by means of advanced *in-situ* methods and theoretical modeling. Dissertation thesis. 2017.
[23] Q. Meng, et. al., *In-Situ* Synchrotron X-Ray Diffraction Investigations of the Nonlinear Deformation Behaviour of a Low Modulus β-Type Ti36Nb5Zr Alloy, Metals 2020, 10(12).
[24] PyFAI. Avaiable from https://pyfai.readthedocs.io/en/v2023.1/biblio.html (cited: 16.03.2024).
[25] LMFIT for Python, VoigtModel. Avaliable from https://lmfit.github.io/lmfit-py/builtin_models.html (cited: 16.03.2024).
[26] K. Hagihara, et. al., Effect of long-period stacking ordered phase on mechanical properties of MG97ZN1Y2 extruded alloy, Acta Mater. 58(19) (2010) 6282-6293.
[27] T. Mayama, et. al., Crystal plasticity of texture development in magnesium alloy during extrusion, Int. J. Plast. (12) (2011) 1916-1935.

[28] G. Garcés, et. al., Combination of in-situ diffraction experiments and acoustic emission testing to understand the compression behavior of Mg-Yzn alloys containing LPSO phase under different loading conditions. *International Journal of Plasticity 106 (2018) 107–128*

[29] S.R. Agnew, et. al., *In-situ* neutron diffraction of a quasicrystal containing Mg alloy interpreted using a new polycrystal plasticity model of hardening due to {10.2} tensile twinning, Int. J. Plastic, 100 (2018) 34-51.

[30] D. Drozdenko, et. al., The yield point phenomenon in ultrafine-grained dilute Mg-Zn-Y alloys. Materials Letters 330 (2023) 133315

List of Abbreviations

a, c…….lattice parameters in a hexagonal close packed structure

BSE……..…..backscattered electrons

CALs…….cluster arranged layers

CE…….…....cast extruded

CI……..…....confidence index

CRSS……...…….…critical resolved shear stress

CYS…….……...…..compression yield strength

DESY….……..…Deutches Electronen-Synchrotron

DRX…..…….…….dynamically recrystalized

EBSD…….…electron backscatter diffraction

ED……...…extrusion direction

FWHM……...…..…full width at half maximum

hcp…….…….....hexagonal closed packed

HEMS…...…..…....High Energy Materials Science

LM……..light microscopy

LPSO……..…….....long-period stacking order

LS……....….....lattice strain

Mg…….…….....magnesium

RS……..…….rapid solidified

RSRC……..rapidly solidified ribbon consolidation

RT…….……..room temperature

SEM……...……scanning electron microscopy

SFs.……....stacking faults

TEM……...transmission electron microscopy

TYS……...…tensile yield strength

UCS……..…….…ultimate compression strength

UTS…..…….....ultimate tensile strength

Y……..……..yttrium

YP…….....yield point

YS……...…….yield strength

Zn……...……zinc